

**Copyright**  
**by**  
**Choongho Yu**  
**2004**

**Nanomaterials Characterization and Bio-chemical Sensing Using  
Microfabricated Devices**

**by**

**Choongho Yu, B.S., M.S.**

**Dissertation**

Presented to the Faculty of the Graduate School of  
The University of Texas at Austin  
in Partial Fulfillment  
of the Requirements  
for the Degree of

**Doctor of Philosophy**

**The University of Texas at Austin**

**August 2004**

**The Dissertation Committee for Choongho Yu  
certifies that this is the approved version of the following dissertation:**

**Nanomaterials Characterization and Bio-chemical Sensing Using  
Microfabricated Devices**

**Committee:**

---

**Li Shi, Supervisor**

---

**Michael D. Bryant**

---

**Frederick F. Ling**

---

**Shaochen Chen**

---

**Dean P. Neikirk**

## **Dedication**

To my parents, wife, and family

## **Acknowledgements**

I would not be able to forget the moments that I struggled for experiments and microfabrication in ETC and Pickle laboratories. It has been very exciting, instructive, and fun even for the moments that I thought frustrating, painful, and discouraging at that time. Without help, support, and encouragement from many persons, I would never have been able to finish this work.

First of all, I gratefully acknowledge my dissertation supervisor, Prof. Li Shi for his inspiration, encouragement, and invaluable comments during the whole work with this dissertation. This dissertation could not have been written without his guidance, research support, and mentoring throughout my doctoral study. I am deeply indebted to him and also truly appreciate giving me the great opportunity to work in the fascinating field of study with a group of energetic people, Jianhua Zhou, Sanjoy Saha, Anastassios Mavrokefalos, Anthony Hayes, Sarah Ruch, Carlos Villalobos, and Prof. Dae-jin Kang in Micro-Nano Scale Thermo-Fluids Lab.

I give a special thanks to Prof. Frederick F. Ling for his guidance and encouragement during my doctoral study as well as reviewing my dissertation. I would also like to express my gratitude to Prof. Michael D. Bryant, Prof.

Shaochen Chen, and Prof. Dean P. Neikirk for their invaluable comments on my dissertation.

I am very grateful to people, Prof. Peter R. C. Gascoyne, Dr. Jody Vykoukal, Dr. Daynene Vykoukal, Dr. Jon Schwartz, and Celine Joyce at UT MD Anderson Cancer Center for the micro flow cytometer project. I am indebted to Prof. Arun Majumdar and Dr. Deyu Li at UC Berkeley for the thermoelectric property measurements of nanostructures, and Prof. Z. L. Wang's group at Georgia Tech for providing nanobelts for the gas sensor project. I also thank for allowing me to use the facility at UT Microelectronic Research Center and Center for Nano and Molecular Science and Technology.

I thank all my colleagues at the University of Texas at Austin, and especially appreciate friendship and support from Sunyoup Lee, Sanghoon Lee, Kwanwoong Gwak, Daejong Kim, Jaegu Yoo, Young-Keun Park, Ji-Hoon Choi, Younghoon Han, and Jaebum Hur during my study at UT.

Finally, it would be impossible to have my research career without my parents' endless love and support, in addition to my wife's love, sacrifice, and encouragement. My family's love and belief in me makes all worthwhile.

# **Nanomaterials Characterization and Bio-chemical Sensing Using Microfabricated Devices**

Publication No. \_\_\_\_\_

Choongho Yu, Ph.D.

The University of Texas at Austin, 2004

Supervisor: Li Shi

A variety of nanostructured materials have been synthesized in recent years. These nanomaterials have potential applications in areas spanning computing, energy conversion, sensing, and biomedicine. Because of size confinement effects, furthermore, these nanomaterials are expected to show very different physical properties from those of their bulk counterparts. The measurement of their properties, however, has been very challenging due to their small dimensions. Similarly, it remains a challenge to detect chemical and biomolecular species due to their small dimensions.

This dissertation presents the development of microelectromechanical systems (MEMS) devices for the characterization of thermophysical properties of nanomaterials and for the detection of chemical species and biological cells.

The thermophysical property of one-dimensional (1D) nanomaterials was measured using a batch-fabricated microdevice consisting of two adjacent symmetric silicon nitride membranes suspended by long silicon nitride beams. Three methods were developed to assemble nanomaterials with the measurement devices. Those three methods include a wet deposition process, an in-situ chemical vapor deposition technique, and an electric-field-assisted assembly method. During the measurement, one membrane is Joule-heated to cause heat conduction through the nanomaterials to the other membrane, allowing for the measurement of thermal conductance and Seebeck coefficient. The electrical conductance can also be measured using the microdevice. The temperature-dependent properties of an individual single-wall carbon nanotubes (SWCNs) and SWCN bundles were measured. Measurement sensitivity, errors, and uncertainty were examined. The obtained thermal conductivity of an individual SWCN is found to be much higher than bundles of SWCNs in the range of 2000-11000 W/m-K at room temperature, in agreement with theoretical predictions. Furthermore, the thermal conductivity of bundles of SWCNs are found to be suppressed by contact resistance between interconnected SWCNs in the bundle.



The microdevice has also been integrated with metal oxide nanobelts for chemical sensing. The sensing mechanism is based on surface oxidation-reduction (redox) processes that change the electrical conductance of the nanobelt. The sensor was found to be highly sensitive to inflammable and toxic gas species including nitrogen dioxide (NO<sub>2</sub>), ethanol, and dimethyl methylphosphonate (DMMP). Furthermore, it eliminated the sensor poisoning effects that have limited the wide use of polycrystalline metal-oxide based sensors. The experiment is a step towards the large scale integration of nanomaterials with microsystems, and such integration via an electric-field-directed assembly approach can potentially enable the fabrication of low-power, ultra-sensitive, and selective integrated nanosensor systems.

The electric field manipulation technique has not only been used to assemble nanomaterials with MEMS, but also been used to focus biological cells in a microfluidic channel for cytometry applications. Flow cytometry is a powerful and versatile method of rapidly analyzing large populations of cells and other particulate or molecular analytes that have been captured on the surface of carrier particles. However, the key components of the system, hydrodynamic focusing and optical systems, make conventional cytometers complex, large, and expensive. To eliminate these drawbacks, a dielectrophoretic particle focusing

technique combined with MEMS is explored to replace the hydrodynamic focusing mechanism.

To focus particles, microelectrodes are patterned on the circumference of the channel to generate AC fringing fields that result in negative dielectrophoretic forces directing cells from all directions to the center of the channel. An elliptic-like microfluidic channel has been fabricated by isotropic etching of soda lime glass wafers and a subsequent wafer-bonding process. Experiments with microbeads and human leukemia HL60 cells and an analysis using a thin shell model indicate that biological cells can be focused using an AC voltage of an amplitude up to  $15 V_{p-p}$  and a frequency below 100 kHz, respectively. This design eliminates the sheath flow and the fluid control system that makes conventional cytometers bulky, complicated, and difficult to operate, and offers the advantages of a portable standalone instrument as well as a module that could potentially be integrated with on-chip impedance or optical sensors into a micro total analysis system.

## Table of Contents

List of Tables .....	xiii
List of Figures .....	xiv
Chapter 1: Introduction.....	1
1.1 Energy transport in low-dimensional nanomaterials.....	1
1.2 Integration of metal oxide nanobelts with microsystems for sensor applications.....	4
1.3 A micro flow cytometer based on dielectrophoretic particle focusing...6	
Chapter 2: Measurement of Thermophysical Properties of One-Dimensional (1D) Nanostructures.....	11
2.1 Device design and fabrication .....	11
2.2 Assembly of nanostructures on the microdevice.....	16
2.3 Measurement method.....	18
2.3.1 Experimental setup.....	18
2.3.2 Measurement scheme.....	21
2.3.2.1 Thermal conductance.....	21
2.3.2.2 Electrical conductance and Seebeck coefficient .....	28
2.3.2.3 Sensitivity of thermal conductance measurement.....	29
2.3.2.4 Errors in thermal conductance measurement.....	34
2.3.2.5 Uncertainty of thermal conductance and conductivity..37	
2.4 Measurement results and discussion.....	39

Chapter 3: Integration of Nanobelts with Microsystems for Chemical Sensing..	46
3.1 Experimental setup.....	47
3.1.1 Sample preparation.....	47
3.1.2 Characterization of the microdevice for sensor applications...	48
3.2 Measurement results and discussion.....	54
Chapter 4: A Three-Dimensional (3D) Dielectrophoretic Particle Focusing Channel for Micro-Cytometry Applications.....	59
4.1 Theoretical background.....	60
4.2 Positive and negative dielectrophoresis.....	62
4.3 Design and fabrication.....	70
4.3.1 Design of dielectrophoretic particle focusing channel.....	70
4.3.2 Fabrication of the dielectrophoretic particle focusing channel.	74
4.4. Experiment.....	79
4.4.1 Sample preparation.....	79
4.4.2 Experimental procedure and results.....	80
Chapter 5: Conclusion.....	89
Bibliography.....	92
Vita .....	101

## List of Tables

Table 1. Uncertainty of thermal conductance ( $G_s$ ) data shown in Fig. 2.11.....38

## List of Figures

Figure 2.1: SEM of a microdevice for thermal property measurements of nanostructures.....	12
Figure 2.2: SEM of Si:Nb resistance heater/thermometer on the membrane of the microdevice.....	13
Figure 2.3: Fabrication process of the microdevice.....	15
Figure 2.4: SEM of (a) a 10-nm-diameter SWCN bundle, (b) a 148-nm-diameter SWCN bundle, (c) a CVD-grown SWCN, and (d) a SnO <sub>2</sub> nanobelt connecting two Pt electrodes on two adjacent suspended membrane.....	17
Figure 2.5: A schematic diagram of the experimental setup for measuring the thermal and thermoelectric properties of a nanostructure.....	19
Figure 2.6: A schematic diagram of the connection of the measurement equipment to the microdevice.....	20
Figure 2.7: A schematic diagram and thermal resistance circuit of the measurement scheme.....	22
Figure 2.8: Normalized first harmonic component of the measured resistance rise of the heating PRT as a function of the frequency of an AC current coupled to the DC heating current.....	27
Figure 2.9: The resistance ( $R_s(I=0)$ ) of the PRT as a function of temperature...31	
Figure 2.10: Thermal conductance, $G_b$ of the five beams supporting one membrane of the microdevice as a function of temperature. Inset: temperature rise in the heating membrane as a function of the DC heating current at $T_0 = 54.95$ K.....	33

Figure 2.11: Thermal conductivities of a 1 to 3-nm-diameter individual CVD SWCN, a 10-nm- and another 148-nm-diameter SWCN bundles, and an individual MWCN in reference Kim <i>et al.</i> (2001).....	41
Figure 2.12: Measured electrical conductivity of a 148-nm- and a 10-nm-diameter SWCN bundle.....	42
Figure 2.13: The thermopower of an individual SWCN and two SWCN bundles as a function of temperature.....	43
Figure 2.14: Thermoelectric figure of merit ( <i>ZT</i> ) of a 148-nm- and a 10-nm diameter SWCN bundle.....	45
Figure 3.1: SEM of a SnO <sub>2</sub> nanobelt assembled on two Pt electrodes of a suspended MEMS device, which was used for thermophysical property measurements of nanostructures. To enhance electrical conductivity and prevent poisoning effect, Pt was deposited on the two contacts using FIB.....	49
Figure 3.2: Temperature rise of the suspended membrane as a function of power consumption of the Pt heater line.....	50
Figure 3.3: Experimental setup to test the nanobelt sensor for (a) NO <sub>2</sub> and Ethanol gas species, (b) DMMP gas species.....	53
Figure 3.4: Response of the as-assembled nanobelt-MEMS sensor to 0.2, 0.5, 0.9, 1.7, and 10 ppm NO <sub>2</sub> balanced with air when the nanobelt temperature was 200 °C. The voltage applied to the nanobelt was 2 V. ....	54
Figure 3.5: Response of the as-assembled nanobelt-MEMS sensor to 125, 83, 250, and 23 ppm ethanol balanced with air when the nanobelt temperature was 150 °C. The voltage applied to the nanobelt was 1.0 V.....	56

Figure 3.6: Response of the as-assembled nanobelt-MEMS sensor to 78 and 53 ppb DMMP balanced with air when the nanobelt temperature was 230 °C. The voltage applied to the nanobelt was 1.5 V.....57

Figure 4.1: A schematic diagram showing the positive and negative dielectrophoretic forces exerted on particles in a nonuniform electric field created by applying voltage to the electrodes (positive voltage: filled electrodes, ground: hollow electrode) .....63

Figure 4.2: The real part of the Clausius-Mossotti factor for a 10- $\mu$ m-diameter latex bead as a function of the frequency of the applied voltage for the different dielectric properties of the medium and the bead. The permittivity and conductivity of the bead are  $2.5\epsilon_0$  and 8  $\mu$ S/cm, respectively. The unit of the conductivity ( $\sigma$ ) is  $\mu$ S/cm in the legend .....66

Figure 4.3: The real part of the Clausius-Mossotti factor as a function of the frequency of the applied voltage for different dielectric properties of a 10- $\mu$ m-diameter biological cell.  $\epsilon_{int}$  and  $\sigma_{int}$  are the permittivity and the electrical conductivity of the cell interior, respectively. The unit for  $C_s$ ,  $G_s$ , and  $\sigma_{int}$  in the legend are mF/m<sup>2</sup>, kS/m<sup>2</sup>, and S/m, respectively. The thickness of the membrane is 5 nm. The permittivity and conductivity of the medium are  $80\epsilon_0$  and 0.056 S/m, respectively.....69

Figure 4.4: A schematic diagram of a microfluidic channel with a micro-electrode array patterned on its circumference for dielectrophoretic particle focusing.....71

Figure 4.5: (a) Simulation results of the magnitude of the electric field ( $E$ ) in a R-Z cross section of the 100- $\mu$ m-diameter channel when a voltage of 7.5 V is applied to the black electrodes and the white electrodes are



grounded. The permittivity and conductivity of the fluid in the channel are  $80 \epsilon_0$  and  $560 \mu\text{m/cm}$ . The field strength is represented by the gray scale bar (b) The  $-\nabla E^2$  vector field. The magnitude of  $-\nabla E^2$  is represented by the gray scale bar.....73

Figure 4.6: A schematic diagram of the fabrication process of the micro-cytometer.....76

Figure 4.7: An optical micrograph of the elliptic channel with the Au/Cr electrode array.....78

Figure 4.8: A schematic diagram of the experimental setup for measuring the width of the particle stream.....81

Figure 4.9: Fluorescence micrographs of the microfluidic channel as particles flow along the channel. (a) No electric field is applied; (b) Particle focusing is initiated after an electric field is applied; (c) Particles are tightly focused at the center of the microfluidic channel.....83

Figure 4.10: The width of a flow stream of microbeads as a function of the applied voltage at different frequencies.....87

Figure 4.11: The width of a flow stream of human leukemia cells as a function of the applied voltage at different frequencies.....88

## Chapter 1: Introduction

This dissertation consists of three experiments that aim to characterize nanomaterials and to detect bio-chemical species using microfabricated devices. This chapter describes the motivation of these experiments.

### 1.1 ENERGY TRANSPORT IN LOW-DIMENSIONAL NANOMATERIALS

Low-dimensional nanomaterials have unique thermophysical properties that may find applications for heat transfer enhancement and efficient thermoelectric energy conversion. Especially, low dimensional nanostructures such as nanotubes, nanowires, and nanobelts can have unique properties very different from those of their bulk counter parts. Several groups have measured Seebeck coefficient (Hone *et al.*, 1998), specific heat (Yi *et al.*, 1999 and Mizel *et al.*, 1999), and thermal conductivities (Hone *et al.*, 1999, 2000) of carbon nanotube (CN) mats, and the thermal conductivities of SiGe superlattice and Si nanowires (Li *et al.*, 2003a and b).

In general, as these nanostructures are confined to low dimensions with a size comparable to the phonon scattering mean free paths, the thermal conductivity is often reduced compared to the bulk values due to increased phonon-boundary scattering and modified phonon dispersion (Li *et al.*, 2003a and b). An exception to this scaling trend is CNs. Due to atomically smooth surface

and low defect concentrations, CNs are expected to have ultra-high thermal conductivity (Berber *et al.* 2000 and Che *et al.*, 2000).

However, the measured thermal conductivities of a multiwall (MW) CN bundle (Yi *et al.*, 1999) and a single wall (SW) CN mat at room temperature (Hone *et al.*, 2000) are about 20 and 250 W/m-K, respectively, orders of magnitude lower than theoretical predictions. The low thermal conductivity is due to large thermal resistance at the junctions between individual tubes in a millimeter-size bundle or mat. Moreover, the filling factor or density of the tubes in the mat is unknown. In addition, the measured thermal conductance increases with temperature for the entire temperature range of 8-350 K, showing no signature of Umklapp phonon-phonon scattering. This indicates that the dominant scattering mechanism is phonon scattering by defects and boundaries. Recently, the thermal conductivity of an individual MWCN has been measured using a microfabricated device. The observed room temperature thermal conductivity is more than 3000 W/m-K (Kim *et al.*, 2001). Meanwhile, SWCNs are expected to have even higher thermal conductivities than MWCNs due to the absence of inter-cell scattering.

Furthermore, a SWCN is an ideal system to study quantum thermal conduction phenomena. For example, a (10, 10) SWCN has a series of phonon sub-bands near the zone center (Dresselhaus and Eklund, 2000). The small

diameter ( $d_t$ ) of the nanotube causes relatively large sub-band splitting. For a temperature  $T \ll 2hv/(k_B d_t)$ , where  $h$ ,  $v$ ,  $k_B$ ,  $d_t$  are Planck constant, phonon group velocity, Boltzmann constant, and tube diameter, respectively, only four acoustic modes are occupied, and the thermal conductance of a SWCN is expected to show linear temperature dependence with a maximum possible value  $G_{th} = 4g_0$ . Here,  $g_0 = \pi^2 k_B^2 T / 3h = (9.456 \times 10^{-13})T$  (W/K) is the universal quantum of thermal conductance (Schwab *et al.*, 2000).

It is of interest to investigate the intrinsic thermal transport properties of individual CNs that are not influenced by contact thermal resistances at the junctions between individual tubes and by phonon scattering between adjacent tubes. However, measuring the thermal conductivity of an individual SWCN is very challenging because the extremely small cross section results in a very small thermal conductance. Therefore, conventional techniques for thin film thermal property measurements, such as the  $3\omega$  method (Cahill, 1990), cannot be used readily for these nanostructures due to the small sample size.

In this dissertation, the thermal and thermoelectric properties of SWCNs have been measured using a microdevice. The nanostructures are deposited between two adjacent membranes of the microdevice using a wet deposition or chemical vapor deposition (CVD) method. A Pt heater/resistance thermometer (PRT) is patterned on each membrane. As one membrane is heated to up to 2-5 K,

heat conduction through the bridged nanostructure causes temperature to rise on the membrane, allowing the measurement of the thermal properties of the nanostructures. The measurement and results for the thermoelectric properties of an individual 1~3-nm-diameter CN as well as a 148-nm and a 10-nm diameter CN bundle are presented in chapter 2.

## **1.2 INTEGRATION OF METAL OXIDE NANOBELTS WITH MICROSYSTEMS FOR SENSOR APPLICATIONS**

The microdevice has also been integrated with metal oxide nanobelts for sensor applications. Metal oxide sensors are commonly used to monitor a variety of toxic and inflammable gases in air pollution monitoring systems, food industry, medical diagnosis equipment, and gas-leak alarms. The sensing mechanism is based on surface oxidation-reduction processes (redox) that change the concentration of oxygen vacancies in the metal oxide and thus alters its electrical conductance (Gardner, 1994 and Morrison, 1994). Because only the surface layer is affected by the reaction, the sensitivity of a metal oxide sensor increases for decreasing thickness, motivating the development of thin film metal oxide sensors with the use of microelectromechanical system (MEMS) technologies (Kovacs, 1998). A key component of the MEMS sensor is a thermally isolated membrane structure with a built-in thin film resistor that is Joule-heated to 150-400 °C. The high temperature enhances the redox processes and improves the sensitivity.

However, when the thickness of a metal oxide film deposited by a physical or chemical vapor deposition method is reduced below 100 nm to achieve the ultimate sensitivity, the film often consists of a high density of pinholes and defects that lead to unstable electrical properties. These problems have prevented the reduction of the film thickness, limiting the sensitivity of thin film metal oxide sensors to a few parts per million (ppm) of gas species. Additionally, grain boundaries in the film are responsible for degradation and poisoning of the sensor, which causes poor repeatability and long term instability.

Recently, belt-like metal oxide nanostructures have been synthesized (Pan *et al.*, 2001 and Dai *et al.*, 2003). These metal oxide nanobelts are single crystalline and structurally uniform. Because the nanobelt can be as thin as 10 nm, almost the entire thickness can be affected by the redox processes with environmental gas species. In an earlier work (Comini *et al.*, 2002), tin dioxide (SnO<sub>2</sub>) nanobelts have been tested for gas sensing. In their work, a bunch of nanobelts were deposited on Au electrodes. When the nanobelt was heated using an external heater, it showed a sub-ppm level sensitivity for detecting nitrogen dioxide (NO<sub>2</sub>) gas. Moreover, the absence of grain boundaries in these single crystalline structures allows for long-term stability and reliability, the lack of which has prevented the wide application of polycrystalline thin film metal oxide sensors.

One of the major challenges for the development of sensor technologies based on “bottom-up” synthesized nanostructures, e.g. carbon nanotubes (Collins *et al.*, 2002 and Shim *et al.*, 2002), semiconductor nanowires (Cui *et al.*, 2001), and metal oxide nanobelts, is the large-scale manufacturing of well-organized nanostructure sensor arrays with the complex functionality comparable to that of MEMS sensors. Examples of such functionality include thermal and flow controls that can be integrated with MEMS sensors.

Chapter 3 describes the integration of single-crystalline nanobelts with microdevices into a low-power, sensitive, and stable sensor. The microdevice provides localized thermal control for the nanobelt, eliminating the need for an external heater that consumes much more power. The experiment is a step towards the large-scale integration of nanomaterials with microsystems, and the integration via the electric field directed assembly method can potentially enable the fabrication of low-power, sensitive, and selective nano-sensor systems.

### **1.3 A MICRO FLOW CYTOMETER BASED ON DIELECTROPHORETIC PARTICLE FOCUSING**

The electric field manipulation method has not only been used to assemble nanostructures, but also used for flow cytometry applications. Flow cytometry is a powerful and versatile method of rapidly analyzing large populations of cells and

other particulate or molecular analytes that have been captured on the surface of carrier particles. This method has been widely used in bioindustrial research and clinical diagnostic applications for the last 40 years (Ormerod, 2000 and Melamed *et al.*, 1991). In practice, particles are focused into a tight stream of  $\sim 25 \mu\text{m}$  in diameter established within a  $\sim 100 \mu\text{m}$ -diameter flow channel. The particle trajectory is coincident with the focus of one or more illumination sources and detectors that are used to determine the light scattering and fluorescence properties of individual particles. From these properties, it is possible to determine particle size and morphology, as well as to identify surface markers or DNA content through the use of fluorescent probes. In conventional cytometers, the key components enabling these functions are hydrodynamic focusing and optical detection systems. The hydrodynamic focusing system uses a sheath fluid medium to focus particles in a fluid suspension within the focal point of the optical system. In addition, the sheath fluid medium prevents impurities or agglomerated clusters from clogging the channel. The optical system excites fluorescently labeled particles and captures photons of selected wavelengths.

The hydrodynamic focusing and optical systems, however, make conventional cytometers complex, large, and expensive. First, the hydrodynamic particle focusing mechanism requires a complicated system for controlling the proper flow rates and mixing of the sheath and sample flows. In addition, a



reservoir is required for the sheath flow medium, which also has to be supplied and kept free of dust and bacteria. The optical system, moreover, is large, expensive, and prone to misalignment from electrical drift, thermal expansion, and vibration. As a result, the system requires constant alignment and preventive maintenance by skilled personnel.

One possible solution to these drawbacks of conventional cytometers is the use of MEMS. Because of their small size, MEMS devices can handle micron-size cells effectively, and can be made inexpensively using a batch-fabrication process. To date, there have been several attempts to fabricate micro flow cytometers using MEMS fabrication techniques. For example, Lee *et al.* reduced the size of the hydrodynamic focusing system of the conventional cytometer by using a hot embossing method (Lee *et al.*, 2001). Huh *et al.* (2002) used air as a sheath fluid medium to eliminate the liquid reservoirs required in conventional cytometers and thereby reduced the volume and weight of the cytometer system. Schrum *et al.* (1999) proposed to use electrokinetic flow rather than a mechanical pump to drive and control the sheath flow. These three designs still require a sheath flow to position the particles within the focus of the optical detection system. A system without the sheath flow has been proposed by Altendorf *et al.* (1997). In their design, a small V-groove constriction was used for focusing the cells. The small channel size, however, requires careful sample preparation to

prevent the channel from becoming clogged.

In this dissertation, dielectrophoretic particle focusing technique was used to replace the hydrodynamic focusing mechanism. In dielectrophoresis, a nonuniform AC electric field induces a dipole moment in a charge-neutral particle, causing the particle to move toward a region of maximum or minimum electric field strength. The driving direction depends on the polarizability of the particle compared with that of the medium surrounding the particle and the frequency of the applied electric field.

It has been shown that dielectrophoresis can be used to manipulate micrometer- and nanometer-scale biological particles. Pethig *et al.* (1992), for example, demonstrated the collection of yeast cells in an interdigitated castellated microelectrode array, and Fuhr *et al.* (1992) demonstrated that biological cells could be levitated, held, and rotated within traps. Huang *et al.* (1993) showed that yeast cells could be made to travel linearly in a microfluidic channel. The principle has further been applied to the fractionation of specific cell types in several dielectrophoresis-based flow systems such as those described by Holmes *et al.* (2000) and Wang *et al.* (2000). In addition, Hughes *et al.* (1998) reported that nanometer-scale viruses can be manipulated by positive and negative dielectrophoresis, and Wang *et al.* (2003) showed that DNA can be focused in a channel using negative dielectrophoresis. Fiedler *et al.* (1998) and Morgan *et al.*

(2003) have developed funnel-shape microelectrodes for focusing micron and nanometer size particles using negative dielectrophoresis. Because the voltage was applied between the top and bottom electrodes, the channel height of their design needed to be as small as 30  $\mu\text{m}$  in order to obtain a sufficiently large focusing force. Most recently, Cheung *et al.* (2004) combined a similar dielectrophoretic focusing channel with impedance detection into a micro-Coulter particle counter.

Here, a new use of the dielectrophoresis in a versatile micro flow cytometer was explored for biological cell analysis. In this design, cells are directed toward the center of a microchannel from all directions by negative dielectrophoretic force generated by the fringing field from microelectrodes patterned on the circumference of an elliptic-like channel. Because the voltage is applied between adjacent electrodes on the channel wall, the channel cross section can be as large as 100  $\mu\text{m}$  to avoid clogging. The device was tested for focusing microbeads and human leukemia HL60 cells. The experiments and an analysis using a thin shell model indicate that biological cells can be focused using an AC voltage of an amplitude of 15  $V_{\text{p-p}}$  and frequency below 100 kHz, respectively. The theoretical background of dielectrophoresis, the design and fabrication of the microcytometer, and the experimental results are discussed in chapter 4.

## **Chapter 2: Measurement of Thermophysical Properties of One-Dimensional (1D) Nanostructures**

A batch-fabricated microdevice has been employed to measure thermophysical properties of 1D nanostructures. The device consists of two adjacent symmetric silicon nitride membranes that are suspended by long silicon nitride beams and a PRT is fabricated on each membrane. One membrane is Joule-heated to cause heat conduction through the sample to the other membrane. Thermal conductance, electrical conductance, and Seebeck coefficient are measured using this microdevice at 30~300 K.

### **2.1 DEVICE DESIGN AND FABRICATION**

Figure 2.1 shows a scanning electron micrograph (SEM) of the microdevice used for the thermophysical property measurements of nanostructures. The device is a suspended structure consisting of two adjacent  $14\ \mu\text{m} \times 25\ \mu\text{m}$  low stress silicon nitride ( $\text{SiN}_x$ ) membranes suspended with five  $0.5\text{-}\mu\text{m}$ -thick,  $420\text{-}\mu\text{m}$ -long and  $2\text{-}\mu\text{m}$ -wide silicon nitride beams. One  $30\text{-nm}$ -thick and  $300\text{-nm}$ -wide PRT coil is designed on each membrane. The PRT is connected to  $200\ \mu\text{m} \times 200\ \mu\text{m}$  Pt bonding pads on the substrate via  $1.8\ \mu\text{m}$  wide Pt leads on

the long  $\text{SiN}_x$  beams. An additional  $1.8\ \mu\text{m}$  wide Pt electrode is designed on each membrane next to each other, providing electrical contact to the sample.

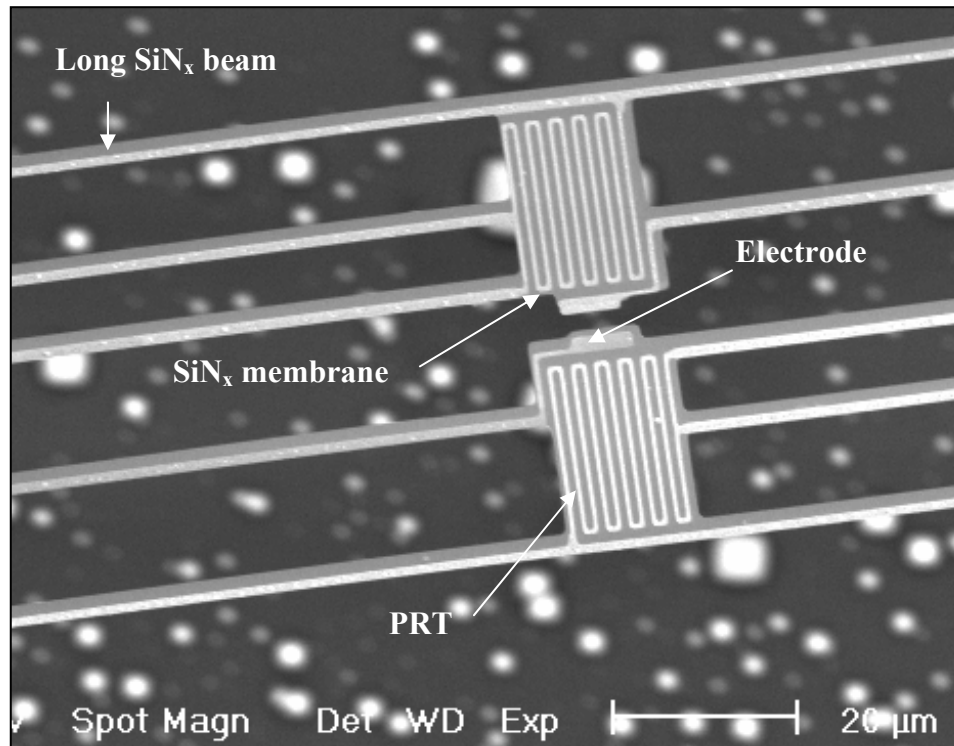


Figure 2.1: SEM of a microdevice for thermal property measurements of nanostructures.

Based on an earlier work (Shi *et al.*, 2003), a new design of the microdevice was also fabricated as shown in Fig. 2.2. In this design, the Pt line is replaced by a Si:Nb with larger temperature coefficient of resistance (TCR).

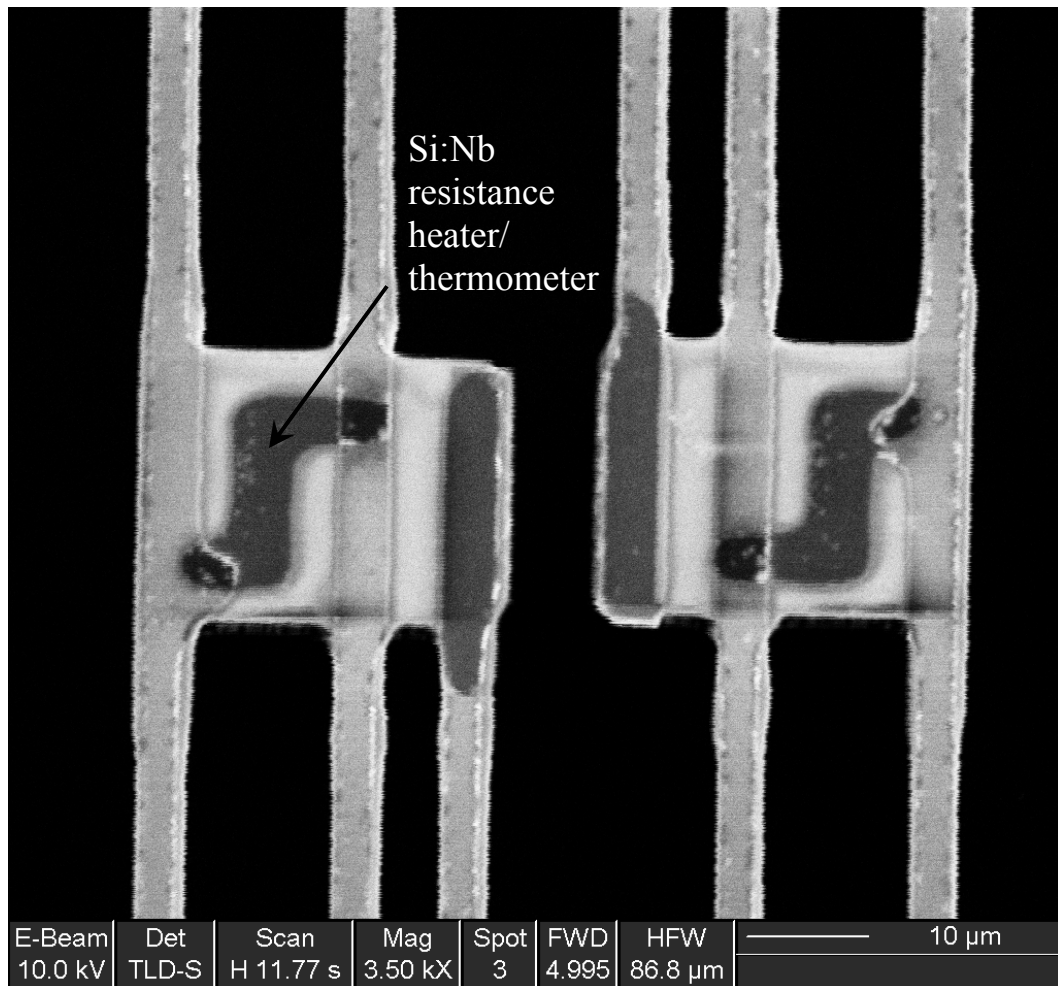


Figure 2.2: SEM of Si:Nb resistance heater/thermometer on the membrane of the microdevice.

The device was batch-fabricated using a 100-mm-diameter Si wafer. First, a 0.5- $\mu\text{m}$ -thick low-stress  $\text{SiN}_x$  film was deposited using a low pressure chemical vapor deposition (LPCVD) method, as shown in Fig. 2.3a. A 10 nm-thick Cr and

subsequently a 40 nm-thick Pt film was deposited on the SiN<sub>x</sub> film by radio-frequency (RF) sputtering. As an etch mask, a 150-nm-thick Si layer was deposited by RF sputtering. A photoresist film was then spun and patterned. The photoresist pattern was transferred to the Si film using reactive ion etching (RIE). Using the patterned Si as a mask, the unprotected Pt film was etched using sputter-etching to make Pt lines (Fig. 2.3b). After the photoresist and Si layers were stripped, a 150-nm-thick Si film co-sputtered with Nb was deposited on the wafer. A photoresist layer was again spun and patterned to create a Si:Nb heater/thermometer using RIE, as shown in Fig. 2.3c. A SiO<sub>2</sub> layer was deposited by plasma enhanced chemical vapor deposition (PECVD). To enhance the adhesion of the film, the wafer was annealed at 500 °C for 20 min and cooled down slowly. A photolithography and RIE step were then used to open contact windows to the Pt contact pads for wire bonding, and to the Pt electrode near the PRT. This Pt electrode was used for making electrical contact to the nanostructure sample. A photoresist film was then spun on the wafer and patterned. The pattern was transferred to the SiN<sub>x</sub> film by RIE (Fig. 2.3d) and the SiN<sub>x</sub> on the backside of the wafer was also stripped by RIE. After the photoresist was stripped, tetramethylammonium hydroxide (TMAH) was used to etch the exposed Si region and the suspended structure was released when the Si substrate was etched away, as shown in Fig. 2.3e.

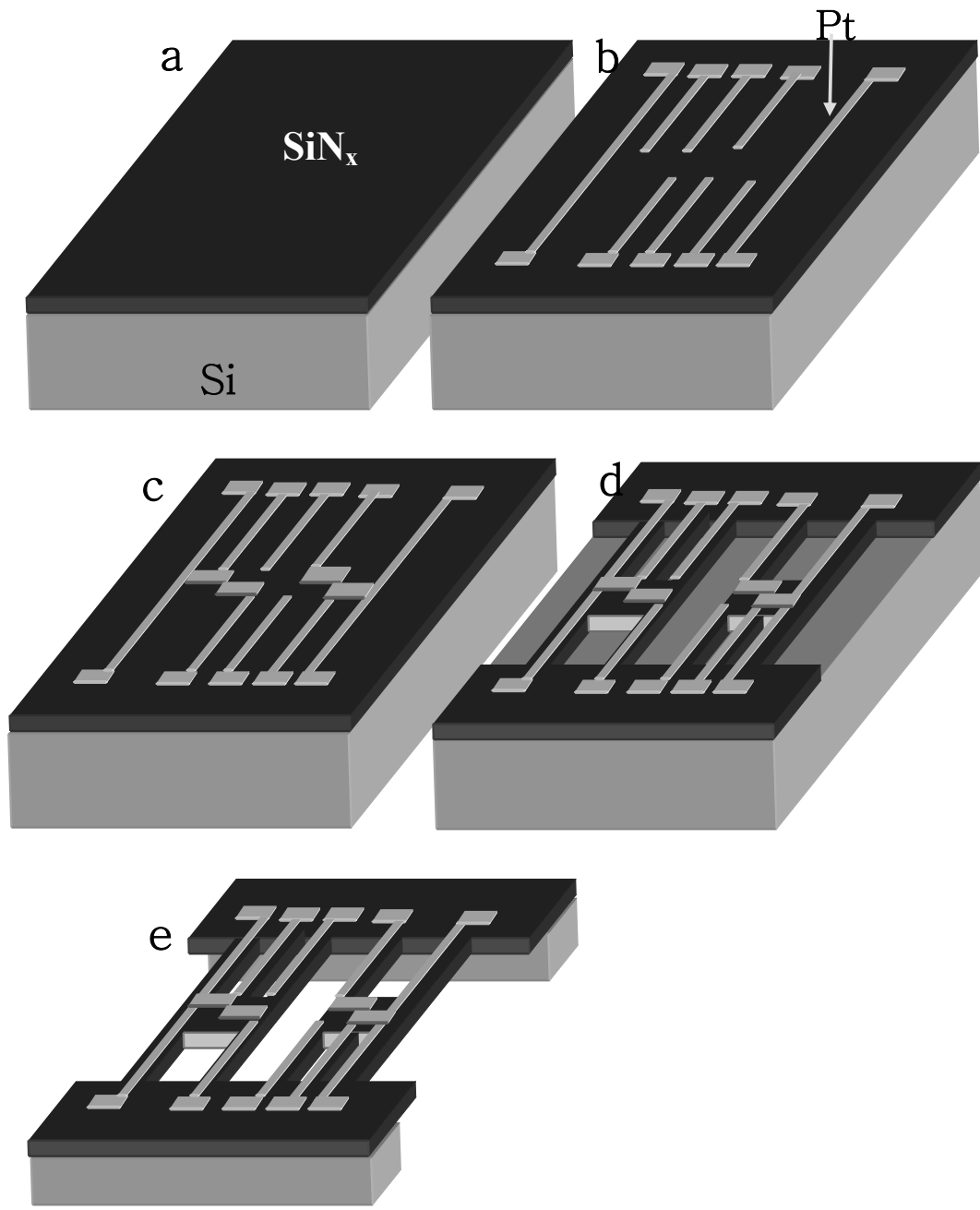


Figure 2.3: Fabrication process of the microdevice.



For accurate measurements of the diameter of an individual SWCN, the SiN<sub>x</sub> layer on the backside of the substrate was stripped and etched in TMAH to create a hole for transmission electron microscopy (TEM) measurement. The etching pit in the Si substrate is either 100-200 μm deep or through the wafer. Using this wafer-stage fabrication technique, about 2000 densely packed suspended structures can be made on a 100 mm diameter wafer.

## **2.2 ASSEMBLY OF NANOSTRUCTURES ON THE MICRODEVICE**

Nanostructures can be placed between the two suspended membranes by using several methods. In the first approach, a solution containing the nanostructures is dropped on a wafer containing many suspended devices. The nanostructures are often adsorbed on the two Pt electrodes. Subsequent spinning the solution off the wafer often leads to the removal of most nanostructures deposited on the wafer, except for those pinned to the two electrodes. Fig. 2.4a, b, and d show a 10-nm-diameter SWCN bundle, a 148-nm-diameter SWCN bundle, and a SnO<sub>2</sub> nanobelt adsorbed on the two membranes, respectively, by using this wet deposition method. To improve the thermal and electrical contact between the sample and the Pt electrode, the device was annealed at 300 °C for a few hours. Further, a small tungsten or Pt pad can be deposited on top of the sample-electrode contact using focused ion beam (FIB) technique. The electron beam with high magnification can further improve the contact because the organic

contamination in the SEM chamber can induce the deposition of a carbon film on the focused region.

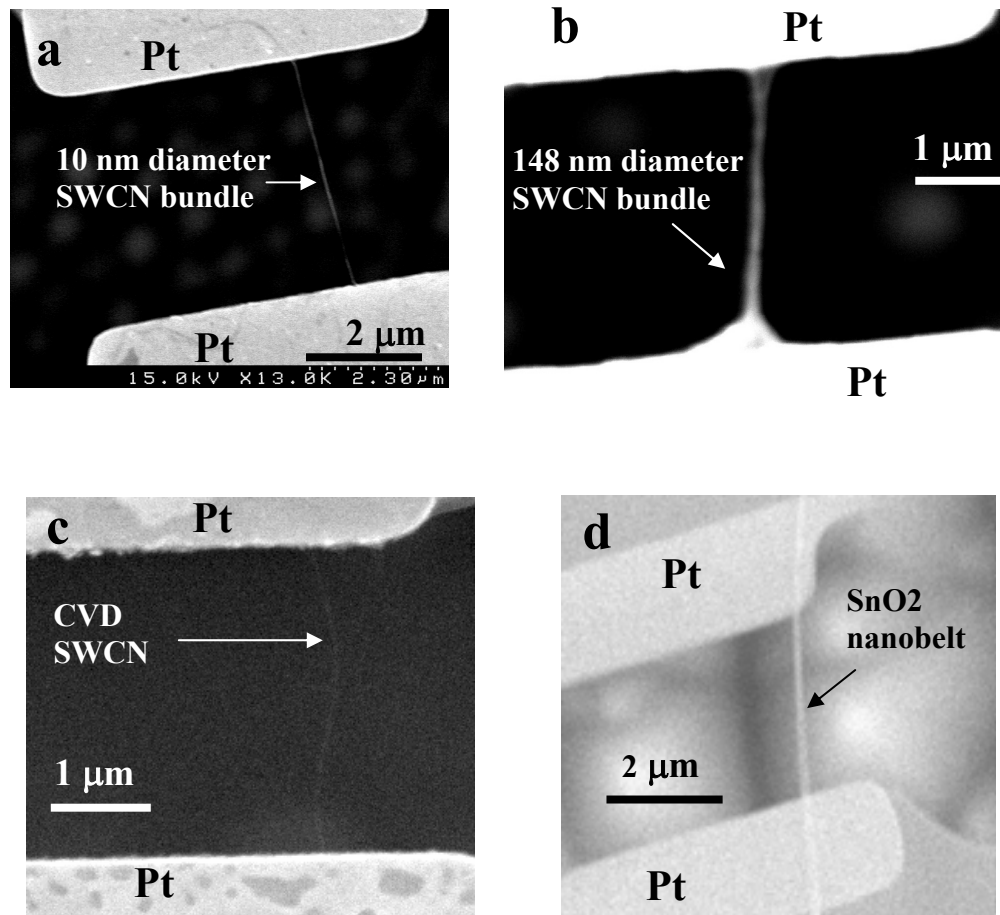


Figure 2.4: SEM of (a) a 10-nm-diameter SWCN bundle, (b) a 148-nm-diameter SWCN bundle, (c) a CVD-grown SWCN, and (d) a SnO<sub>2</sub> nanobelt connecting two Pt electrodes on two adjacent suspended membranes.

In the second approach, a CVD method was used to grow individual SWCNs bridging the two membranes. First, nano-particle catalysts made of Fe, Mo and Al<sub>2</sub>O<sub>3</sub> were placed on the contact pads of the membranes using a probe station. Then, the suspended device was placed in a 900°C CVD tube with flowing methane, yielding individual SWCNs grown between two catalyst particles on the two Pt electrodes. Figure 2.3c shows SWCNs synthesized by this method. The sample-electrode contact was annealed in the high-temperature growth process, leading to low contact resistance.

## **2.3 MEASUREMENT METHOD**

### **2.3.1 Experimental setup**

Figure 2.5 shows the schematic diagram of the experimental setup for measuring the thermoelectric properties of nanostructures. The microdevice was placed in a cryostat with a vacuum level better than  $1 \times 10^{-5}$  Torr. The temperature of the microdevice was cooled by liquid nitrogen (LN) or liquid helium (LHe), and stabilized at a specific point by the heater of the temperature controller. The device was connected to two SR830 lock-in amplifiers and a data acquisition (DAQ) board.

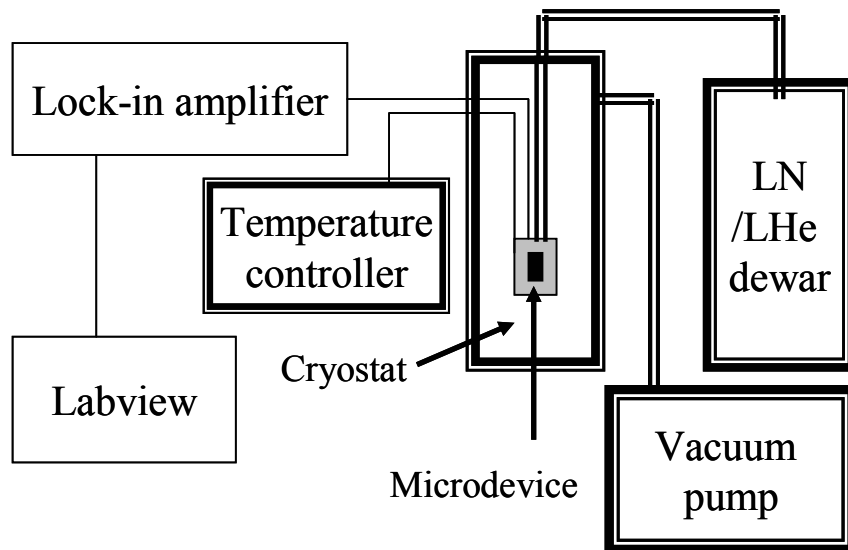


Figure 2.5: A schematic diagram of the experimental setup for measuring the thermal and thermoelectric properties of a nanostructure.

Figure 2.6 describes the connection of the measurement equipment to the microdevice. For thermal conductance measurements of nanostructures, one of the heater lines was coupled to DC current ( $V_{out}$ : Ch0) using a DAQ board to raise the temperature of the lower membrane (from D to A). Meanwhile, to measure temperature rises in the membranes, AC current was passed through the heater lines (from D to A and from G to K) and voltage drops across the lines were measured between B and C, and H and J. To measure the Seebeck coefficient of nanostructures, a voltage difference across the nanostructure (E and F) was measured by using a voltage amplifier.

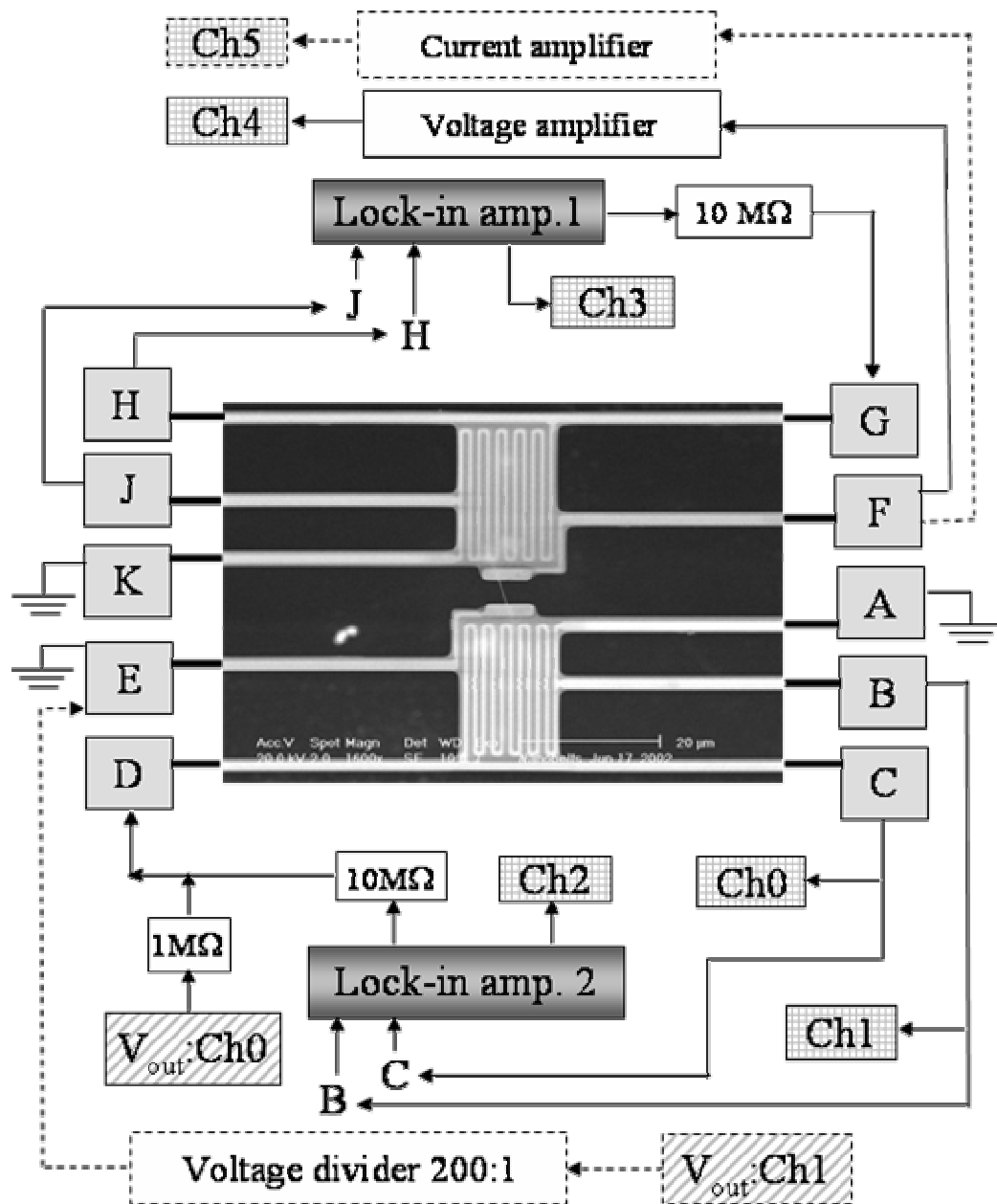


Figure 2.6: A schematic diagram of the connection of the measurement equipment to the microdevice.

In addition, the electrical conductance of the nanostructure was measured using a DC current supplied (from E to F) using a DAQ output port ( $V_{\text{out}}$ : Ch1) with a current amplifier. All data were recorded to Ch0~5.

## 2.3.2 Measurement scheme

### 2.3.2.1 Thermal Conductance

The setup for measuring the thermal conductance of nanostructures is shown in Fig. 2.7. The two suspended membranes are denoted as the heating membrane and sensing membrane, respectively.

A DC current ( $I$ ) flows to one of the two PRTs. Joule heat  $Q_h = I^2 R_h$  is generated in this heating PRT that has electrical resistance  $R_h$ . The PRT on each membrane is connected to the contact pads by four Pt leads, allowing four-probe resistance measurements. The resistance of each Pt lead is  $R_L$ , which is about half of  $R_h$ . A Joule heat of  $2Q_L = 2I^2 R_L$  is dissipated in the two Pt leads that supply the DC current to the heating PRT. We can assume that the temperature of the heating membrane is raised to a uniform temperature  $T_h$ . This assumption can be justified because the internal thermal resistance of the small membrane is much smaller than the thermal resistance of the long narrow beams thermally connecting the membrane to the silicon chip at  $T_\theta$ , the temperature of the environment. A certain amount of the heat  $Q_2$  is conducted through the sample from the heating

membrane to the sensing membrane, raising the temperature of the sensing membrane to  $T_s$ .

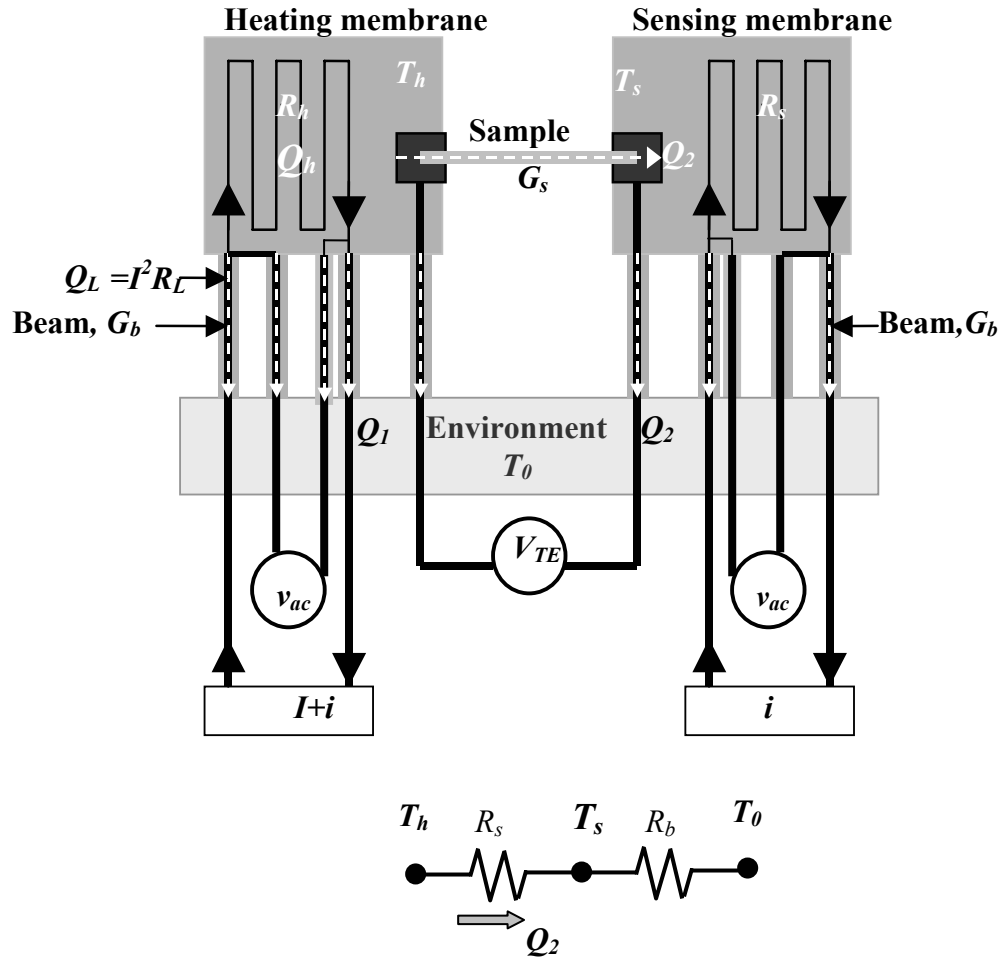


Figure 2.7: A schematic diagram and thermal resistance circuit of the measurement scheme.

In vacuum and with a small  $\Delta T_h$  ( $\equiv T_h - T_0 < 2\text{K}$ ), the heat transfer between the two membranes by air conduction and radiation is negligible compared to  $Q_2$  through the sample, as discussed below. The heat flow in the amount of  $Q_2$  is further conducted to the environment through the five beams supporting the sensing membrane. The rest of the heat, i.e.  $Q_1 = Q_h + 2Q_L - Q_2$ , is conducted to the environment through the other five beams connected to the heating membrane.

The five beams supporting each membrane are designed to be identical. It can be shown that below 400 K, the radiation and air conduction heat losses from the membrane and the five supporting beams to the environment are negligible compared to conduction heat transfer through the five beams. Hence, the total thermal conductance of the five beams can be simplified as  $G_b = R_b^{-1} = 5k_l A/L$ , where  $k_l$ ,  $A$ , and  $L$  are the thermal conductivity, cross sectional area, and length of each beam, respectively. We can obtain the following equation from the thermal resistance circuit shown in Fig. 2.7,

$$Q_2 = G_b(T_s - T_0) = G_s(T_h - T_s), \quad (2.1)$$

where  $G_s$  is the thermal conductance of the sample, consisting of the intrinsic thermal resistance of the nanostructure sample and the contact thermal resistance between the sample and the two membranes, i.e.

$$G_s = \frac{1}{R_s} = (G_n^{-1} + G_c^{-1})^{-1} \quad (2.2)$$



where  $G_n = k_n A_n / L_n$  is the intrinsic thermal conductance of the nanostructure,  $k_n$ ,  $A_n$ , and  $L_n$  are the thermal conductivity, cross sectional area, and length of the sample segment between the two membranes, respectively.  $G_c$  is the contact thermal conductance between the nanostructure and the two membranes. Because the temperature excursion  $\Delta T_h$  is small,  $G_s$ ,  $G_b$ , and  $G_c$  are assumed to be constant as  $\Delta T_h$  is ramped up.

Considering one dimensional heat conduction, we can obtain the temperature distribution in the ten beams supporting the two membranes. A Joule heat of  $Q_L$  is generated uniformly in each of the two beams supplying the heating current, yielding a parabolic temperature distribution along the two beams; while linear temperature distribution is obtained for the remaining eight beams without Joule-heating. The heat conduction to the environment from the two Joule-heated beams can be derived as  $Q_{h,2} = 2(G_b \Delta T_h / 5 + Q_L / 2)$ ; while that from the remaining three beams connected to the heating membrane is  $Q_{h,3} = 3G_b \Delta T_h / 5$ , and that from the five beams connected to the sensing membrane is  $Q_{s,5} = 5G_b \Delta T_s / 5$ , where  $\Delta T_j \equiv T_j - T_0$ ,  $j = h, s$ . Considering energy conservation, i.e.  $Q_{h,2} + Q_{h,3} + Q_{s,5} = Q_h + 2Q_L$ , we can express  $G_b$  and  $G_s$  as a function of  $\Delta T_h$ ,  $\Delta T_s$ ,  $Q_h$ , and  $Q_L$ , i.e.,

$$G_b = \frac{Q_h + Q_L}{(\Delta T_h + \Delta T_s)}, \quad (2.3a)$$

and from Eq. 2.1,

$$G_s = G_b \frac{\Delta T_s}{\Delta T_h - \Delta T_s}. \quad (2.3b)$$

$Q_h$  and  $Q_L$  can be calculated readily from the DC current and the voltage drops across the heating PRT and the Pt leads.  $\Delta T_h$  and  $\Delta T_s$  are calculated from the measured resistance of the two PRTs and their TCR ( $\equiv (dR/dT)/R$ ). The four-probe differential electrical resistance  $R_s$  of the sensing PRT is measured using a SR830 lock-in amplifier with a 250-500 nA 199 Hz sinusoidal excitation current. The temperature rise  $\Delta T_s$  of the sensing membrane depends on the DC current  $I$  of the heating PRT, and is related to  $R_s$  according to the following equation

$$\Delta T_s(I) = \frac{\Delta R_s(I)}{\frac{dR_s(I=0)}{dT}}; \Delta R_s(I) \equiv R_s(I) - R_s(I=0) \quad (2.4)$$

To measure the temperature rise in the heating membrane, a 250-500 nA sinusoidal current  $i_{ac}$  with a frequency  $f$  was coupled to the much larger DC heating current  $I$ . A SR830 lock-in amplifier is used to measure the first harmonic component ( $v_{ac}$ ) of the voltage drop across the heating PRT, yielding the differential resistance  $R_h = v_{ac}/i_{ac}$ . For  $R_h$  obtained by this method, it can be shown that

$$\Delta T_h(I) = \frac{\Delta R_h(I)}{3 \frac{dR_h(I=0)}{dT}}, \text{ for } f \ll 1/(2\pi\tau) \quad (2.5a)$$

$$\Delta T_h(I) = \frac{\Delta R_h(I)}{\frac{dR_h(I=0)}{dT}}, \text{ for } f \gg 1/(2\pi\tau) \quad (2.5b)$$

where  $\tau$  is the thermal time constant of the suspended device, and is estimated to be on the order of 10 ms. The difference between these two solutions originates from a first harmonic modulated heating term, i.e.  $i_{ac}IR_h$ . At a very low (high) frequency compared to  $1/(2\pi\tau)$ , the  $i_{ac}IR_h$  modulated heating yields a nontrivial (trivial) first harmonic component in  $T_h$ . This further causes a nontrivial (trivial) first harmonic oscillation in  $R_h$ . This effect gives rise to a factor of 3 difference in  $\Delta R_h$  measured by the lock-in method. In addition,  $\tau$  is proportional to  $C/K$ , where  $C$  and  $K$  are the heat capacity and thermal conductivity, respectively. According to the kinetic theory,  $K$  is proportional to  $Cl$ , where  $l$  is the phonon mean free path and increases with decreasing temperature. Hence,  $\tau$  is proportional to  $1/l$  and decreases with decreasing temperature. Therefore, the transition between the two solutions in Eq. 2.5 occurs at a higher frequency as the temperature is lowered. This frequency dependence has been confirmed by an experiment conducted at four different temperatures, namely 15 K, 25 K, 100 K, and 300 K, as shown in Fig. 2.8. In the experiment,  $\Delta R_h$  was measured at different  $f$  for the same  $I$  and thus the same  $\Delta T_h$ , and the measurement results exhibit a factor of three difference between the low and high frequency limits, as expected from Eq. 2.5. In practice,

we use  $f = 511$  Hz, for which Eq. 2.5b is valid in the temperature range of 4-400 K.

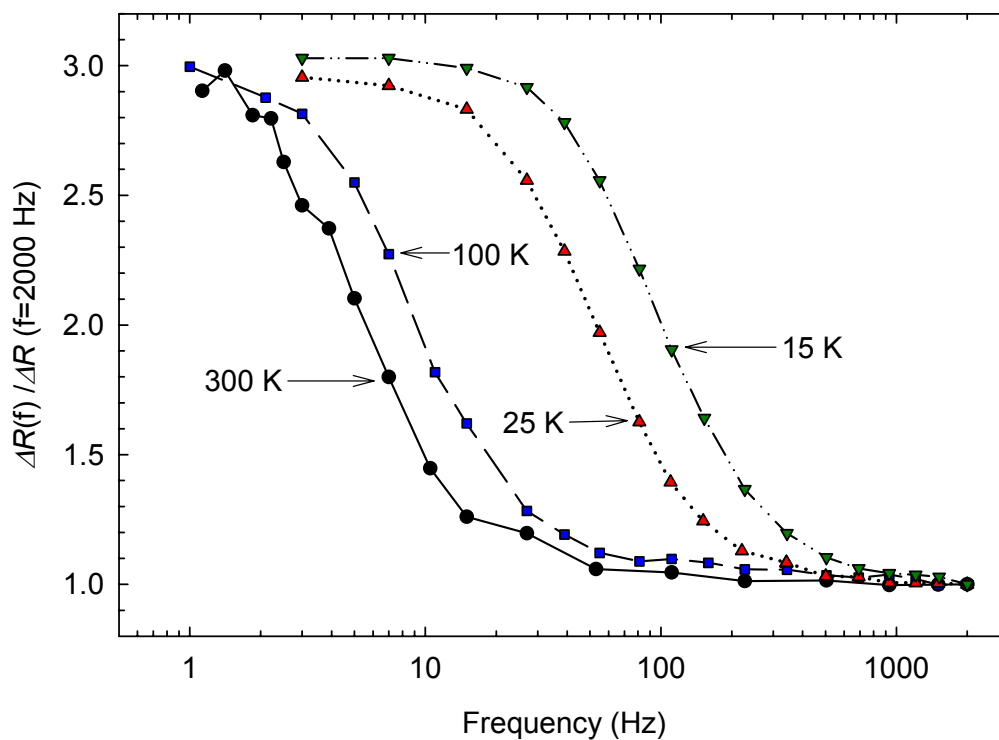


Figure 2.8: Normalized first harmonic component of the measured resistance rise of the heating PRT as a function of the frequency of an AC current coupled to the DC heating current.

### ***2.3.2.2 Electrical Conductance and Seebeck Coefficient***

The electrical conductance of the sample can be measured using two Pt electrodes contacting the two ends of the sample. As mentioned above, a FIB method can be used to deposit a metal line on top of the sample-electrode contact to reinforce the electrical contact and minimize the contact electrical resistance. The FIB deposition can break through the oxide layer of a semiconductor nanowire to reduce the contact resistance.

The Seebeck coefficient, or thermopower, of the SWCN was measured simultaneously with the thermal conductivity. The temperature difference of the two membranes yields a thermoelectric voltage that can be measured using the two Pt electrodes contacting the nanostructure. For each environment temperature ( $T_0$ ), the thermoelectric voltage between the two ends of a nanostructure was recorded when the power input to the heating island was ramped up as shown in Fig. 2.7. The voltage,  $V_{TE}$  was increased linearly with power and thus also linearly with the temperature difference between the two membranes. The slope  $dV_{TE}/dT$  is the Seebeck coefficient. Note that the measurements using the microdevice yield the difference in Seebeck coefficient between the sample and the Pt electrode, i.e.  $S_s - S_{Pt}$ , where  $S_s$  and  $S_{Pt}$  are the Seebeck coefficient of the nanostructure and that of Pt, respectively. The magnitude of  $S_{Pt}$  is typically 5  $\mu\text{V}/\text{K}$  at 300 K and decreases linearly with temperature (Rowe, 1995). These

values are much smaller than the measurement results of  $S_s$ - $S_{Pt}$ . Hence,  $S_s$ - $S_{Pt} \approx S_s$ . By measuring  $T_h$ ,  $T_s$ , and  $V_{TE}$ , the Seebeck coefficient  $S_s$  of the sample can be obtained.

### 2.3.2.3 Sensitivity of Thermal Conductance Measurement

The sensitivity of thermal conductance measurement determines the minimum or noise-equivalent sample thermal conductance that can be measured using the microdevice. From Eq. 2.3b, the noise-equivalent sample thermal conductance ( $NEG_s$ ) that can be measured is proportional to the noise-equivalent temperature rise ( $NET$ ) of the sensing membrane, i.e.

$$NEG_s \approx G_b \frac{NET}{\Delta T_h - \Delta T_s} \quad (2.6)$$

$NET$  is further related to the noise equivalent resistance ( $NER$ ) in the  $R_s$  measurement

$$NET = \frac{NER / R_s}{TCR} \quad (2.7)$$

For the resistance measurement method using a lock-in amplifier,

$$\frac{NER}{R_s} = \frac{\delta v}{v} + \frac{\delta i}{i} \quad (2.8)$$

where  $\delta v$  and  $\delta i$  are the noises in the AC voltage measurement and that of the current source, respectively. At 300 K,  $\delta v$  is dominated by the thermal or Johnson

noise to be  $\delta v = \sqrt{4k_B TR_s \Delta f} \approx 4 \text{ nV}$  for a noise bandwidth of  $\Delta f \approx 0.3 \text{ Hz}$ .

Therefore

$$\frac{\delta v}{v} = \frac{4 \text{ nV}}{2 \text{ mV}} = 2 \times 10^{-6} \quad (2.9)$$

The current source  $i = v_{out}/R$ , where  $v_{out}$  is a sinusoidal 199 Hz output voltage from the lock-in amplifier and  $R$  is the 10 M $\Omega$  resistance of a 10 ppm/K precision resistor that is coupled to the sinusoidal voltage output of the lock-in amplifier for converting a constant AC voltage source to a constant AC current source.

Therefore,

$$\frac{\delta i_{AC}}{i_{AC}} = \frac{\delta v_{out}}{v_{out}} + \frac{\delta R}{R} \quad (2.10)$$

The noise in the AC voltage output from the lock-in amplifier ( $\delta v_{out}/v_{out}$ ) is about  $4 \times 10^{-5}$ . The resistance fluctuation  $\delta R/R$  of the 10 M $\Omega$  precision resistance is about  $2 \times 10^{-6}$  for a 0.2 K fluctuation of room temperature. Therefore,  $\delta i_{AC}/i_{AC} \sim 4.2 \times 10^{-5}$ . The noise in the current source is the dominant noise source. From Eqs. 2.8-10, we can write

$$\frac{NER}{R_s} \approx 5 \times 10^{-5} \quad (2.11)$$

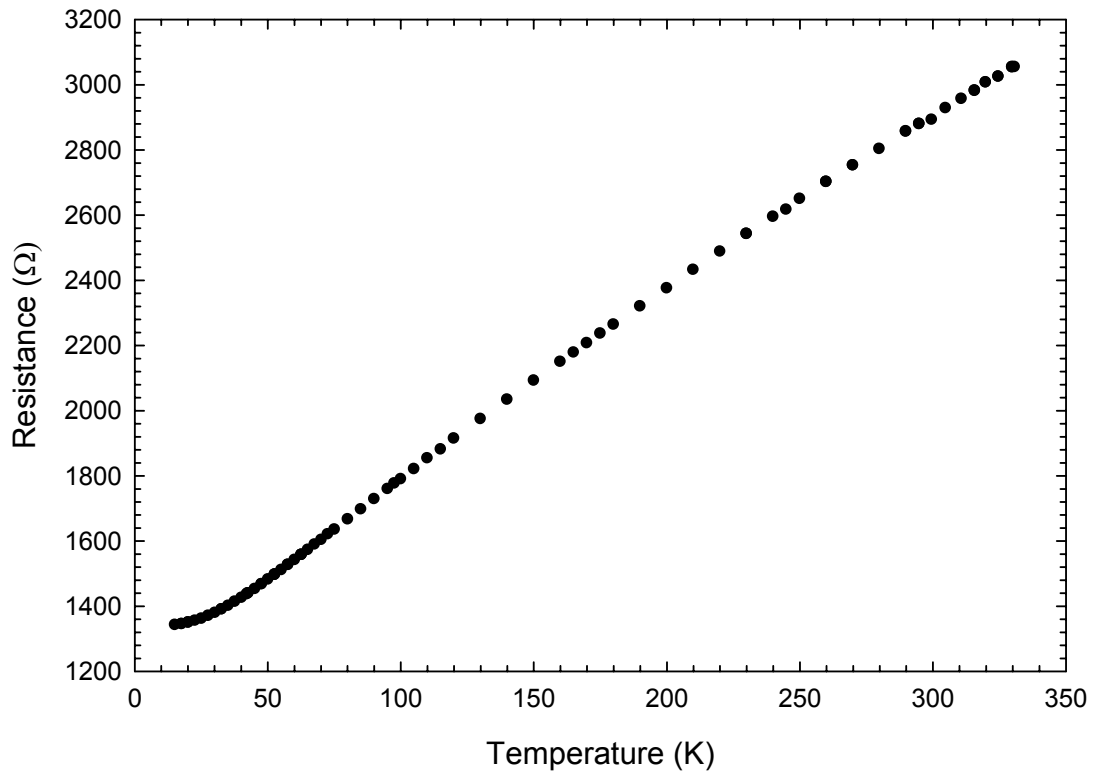


Figure 2.9: The resistance ( $R_s(I=0)$ ) of the PRT as a function of temperature.

This has been confirmed by measuring the noise level using a  $2\text{ K}\Omega$  precision resistor to replace the PRT. The measured resistance noise is about  $100\text{ m}\Omega$ , indicating  $NER / R_s \approx 5 \times 10^{-5}$ .

$R_s(I=0)$  was measured in the temperature range of 10-400 K, as shown in Fig. 2.9. Above 30 K,  $R_s(I=0)$  increases linearly with temperature. Typically, the TCR of the PRT is in the range of  $1.8 \times 10^{-3} - 3.6 \times 10^{-3}\text{ K}^{-1}$  and  $3.5 \times 10^{-3} - 7.2 \times 10^{-3}$



$K^{-1}$  at 300 K and 30 K, respectively, depending on the thin film deposition condition. Thus, *NET* of the lock-in measurement is in the range of 13-27 mK and 6-13 mK at 300 K and 30 K, respectively. Below 30 K, the TCR decreases, leading to a larger *NET*. This *NET* value was found to be comparable or slightly below the temperature fluctuation of the cryostat, which can be controlled to be within 25 mK for  $T_0 > 100$  K and 10 mK for  $T_0 < 100$  K. Therefore,

$$NET \approx 25 \text{ mK for } T_0 = 300 \text{ K}; \quad NET \approx 10 \text{ mK for } T_0 = 30 \text{ K} \quad (2.12)$$

The thermal conductance  $G_b$  of the five beams has been calculated from the measured  $\Delta T_h$  and  $\Delta T_s$  according to Eq. 2.3a. The measured  $\Delta T_h$  is shown in the inset of Fig. 2.10 as a function of  $I$ , and the calculated  $G_b$  is shown in Fig. 2.10. At 300 K,  $G_b$  is about  $9.4 \times 10^{-8}$  W/K, in agreement with the value of  $9.5 \times 10^{-8}$  W/K that is obtained based on the geometry of the beams as well as the room temperature thermal conductivity values of  $\text{SiN}_x$  and Pt films, i.e.  $k_{\text{SiN}_x} = 5.5$  W/m-K and  $k_{\text{Pt}} = 70$  W/m-K.

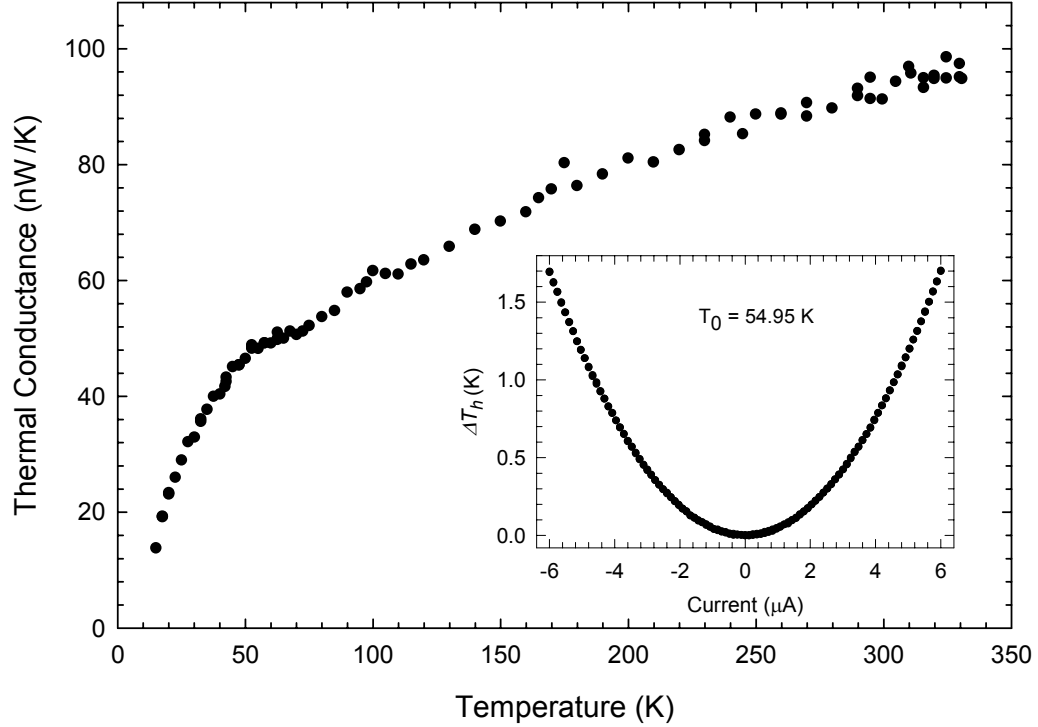


Figure 2.10: Thermal conductance,  $G_b$  of the five beams supporting one membrane of the microdevice as a function of temperature. Inset: temperature rise in the heating membrane as a function of the DC heating current at  $T_0 = 54.95$  K.

Therefore, from Eqs. 2.6 and 2.12, the noise equivalent thermal conductance at 300 K is  $NEG_s \approx 1 \times 10^{-9}$  W/K for a temperature excursion  $\Delta T_h - \Delta T_s = 2$  K. At 30 K,  $G_b \approx 3 \times 10^{-8}$  W/K, and  $NEG_s \approx 1.5 \times 10^{-10}$  W/K for the same temperature excursion. If only the four acoustic phonon modes are filled up for a (10, 10) SWCN at 30 K, the maximum possible thermal conductance would be  $G_{SWCN} = 4$

$g_0 = 4 \times 30 \times 8.9 \times 10^{-13} \text{ W/K} = 1.2 \times 10^{-10} \text{ W/K}$ . This is in the vicinity of the measurement sensitivity. To increase the signal, two or more individual SWCNs can be grown between the two suspended membranes using the CVD method, or an Nb doped Si resistance thermometer with a larger TCR (De Vecchio, 1995) can be used to replace the PRT.

#### **2.3.2.4 Errors in thermal conductance measurement**

One source of the measurement errors is due to heat transfer from the heating membrane to the sensing one via radiation and air conduction. The radiation thermal conductance can be estimated as

$$G_{h-s\_rad} = \sigma(T_s + T_h)(T_s^2 + T_h^2)F_{h-s}A \quad (2.13)$$

where  $F_{h-s}$  and  $A$  are the view factor between the two adjacent membranes and the surface area of one membrane, respectively. It can be shown that  $F_{h-s}A \approx 12 \mu\text{m}^2$ . Thus  $G_{h-s\_rad} = 8 \times 10^{-14}$  and  $7 \times 10^{-11} \text{ W/K}$  at  $T = 30 \text{ K}$  and  $300 \text{ K}$ , respectively. These values are well below the measurement sensitivity.

The thermal conductance of air can be written as  $G_{h-s\_air} = k_a A_{eq} / D$ , where  $k_a$  is the thermal conductivity of the residual air molecules in the cryostat,  $A_{eq}$  and  $D$  are the equivalent surface area of the membrane and the distance between the two membranes, respectively. For a vacuum level  $p = 1 \times 10^{-5} \text{ Torr} =$

$1.33 \times 10^{-2}$  Pa, the mean free path of air molecules is of the order of 1 m and is much larger than  $D$ . Under such circumstance, according to the kinetic theory,

$$k_a = \frac{CvD}{3} \quad \text{and} \quad G_{h-s\_air} = \frac{CvA_{eq}}{3} \quad (2.14)$$

where  $C$  and  $v$  are the heat capacity and velocity of air molecules. From Eq. 2.14, it can be estimated that  $G_{h-s\_air} = 2 \times 10^{-12}$  W/K at  $T = 300$ K, well below the measurement sensitivity of  $1 \times 10^{-9}$  W/K.

The thermal conductance due to air conduction and radiation was measured at different temperatures using a bare device without a nanostructure sample bridging the two membranes. No signal above the noise level can be detected by the sensing PRT as the temperature of the heating membrane is raised. The measurements confirm that air conduction and radiation do not introduce noticeable errors in our measurements.

A major error source in the measurement is the contact thermal resistance,  $R_c \equiv G_c^{-1}$ . To decrease  $R_c$ , as discussed in the previous section, one can deposit a small Pt or W pad on top of the sample-electrode contact so that the sample is sandwiched between two metal layers. Note that the contact area between the sample and the electrode is proportional to the diameter of the nanostructure sample; while the thermal conductance of the sample is proportional to the square of the diameter. Therefore, as a general trend, the ratio of  $G_c$  to  $G_n$  is larger as the

sample diameter becomes smaller. Since  $G_s = (G_c^{-1} + G_n^{-1})^{-1}$ ,  $G_s \approx G_n$  if  $G_c \gg G_n$ .

For this reason, the contact thermal resistance causes a smaller error at nanoscale than at macroscale.

In a measurement of Si nanowires, the error introduced by the contact thermal resistance has been estimated (Li, 2003b). In that measurement, amorphous carbon was deposited on the contact area. The conductance of the contacts and the wire can be expressed as  $k_c A_c / \delta_a$  and  $k_w A_w / L_w$ , where  $k_c$  and  $k_w$  are the thermal conductivities of the amorphous carbon and the nanowire, respectively;  $A_c$  is the contact area and is of the order of  $2\pi r L_c$ , where  $L_c$  is the length of the carbon deposit and is about 2  $\mu\text{m}$ ;  $A_w$  is the cross section area of the nanowire, i.e.  $\pi r^2$  with  $r$  being the radius of the nanowire;  $\delta_a$  is the average distance between the nanowire surface and Pt electrode, which is of the same order of  $r$ , and  $L_w$  is the length of the free-standing segment of the nanowire and is larger than 4  $\mu\text{m}$ . For a 100 nm Si nanowire,  $G_c/G_n$  can be estimated as  $6400 k_c/k_n$ . With  $k_c$  taken to be 0.1 W/m-K, the lower limit of inorganic solid materials, and  $k_n = 47$  W/m-K, the room temperature measurement value of the Si nanowire. Using these values,  $G_c/G_n$  can be estimated as 13.6. Hence, the two contacts together yielded an error less than 15% for the 100 nm Si nanowire. This error due to contact resistance is expected to be smaller for smaller nanowires.

Nevertheless, it is desirable to quantify the contact thermal resistance  $G_c$ . A conventional method is to measure a collection of samples with the same diameter and different lengths. The contact thermal resistance can be estimated from the length-dependence of the sample thermal conductance ( $G_s$ ) provided that thermal conduction in the sample is diffusive.

### 2.3.2.5 Uncertainty of thermal conductance and conductivity

The uncertainty of the measured thermal conductance of the sample can be derived using Eq. 2.3 and  $Q=Q_h+Q_L$ .

$$G_s = \frac{Q \Delta T_s}{(\Delta T_h)^2 - (\Delta T_s)^2} \quad (2.15)$$

$$\begin{aligned} \delta G_s = & \frac{\delta Q \Delta T_s}{(\Delta T_h)^2 - (\Delta T_s)^2} + \frac{2 Q \Delta T_s \Delta T_h \delta(\Delta T_h)}{((\Delta T_h)^2 - (\Delta T_s)^2)^2} + \frac{Q \delta(\Delta T_s)}{(\Delta T_h)^2 - (\Delta T_s)^2} \\ & + \frac{2 Q (\Delta T_s)^2 \delta(\Delta T_s)}{((\Delta T_h)^2 - (\Delta T_s)^2)^2} \end{aligned} \quad (2.16)$$

Considering  $\Delta T_h \gg \Delta T_s$  in the measurements, Eq. 2.16 can be written as

$$\frac{\delta(G_s)}{G_s} = \frac{\delta(Q)}{Q} + \frac{\delta(\Delta T_s)}{\Delta T_s} + 2 \frac{\delta(\Delta T_h)}{\Delta T_h} \quad (2.17)$$

where  $\delta(x)$  is the uncertainty in  $x$ . The dominant term in the right hand side of Eq. 2.17 is  $\delta(\Delta T_s)/\Delta T_s$ . With  $dR_s(I=0)/dT$  obtained from Fig. 2.9 and considering a 1% gain accuracy of the lock-in amplifier, the upper limit of  $\delta(\Delta T_s)$  from Eq. 2.4 is 36

mK. Further,  $\Delta T_s$  depends on the sample thermal conductance. For the 148-nm-diameter SWCN bundle shown in Fig. 2.4b,  $\Delta T_h$  was ramped up to 2 K in the measurement and  $G_s \approx 0.2G_b$  at 300K. Hence,  $\Delta T_s$  was as high as 0.4 K, and  $\delta G_s/G_s \approx \delta(\Delta T_s)/\Delta T_s \approx 9\%$  at 300K. At 30 K,  $G_s \approx 0.05G_b$ , so that  $\Delta T_s \approx 0.1$  K. This results in  $\delta G_s/G_s \approx \delta(\Delta T_s)/\Delta T_s \approx 36\%$  at 30K. For the 10-nm-diameter SWCN bundle shown in Fig. 2.4a,  $\Delta T_h$  was ramped up to 6 K in order to keep the uncertainty  $\delta G_s/G_s$  below 36% and 57% at 300 K and 160 K, respectively. These uncertainty values are summarized in Table 1. They represent the upper bound because they are estimated using the upper limit of  $\delta(\Delta T_s)$ . One way to reduce the uncertainty values is to replace the PRT with a resistance thermometer with a larger TCR.

Table 1. Uncertainty of thermal conductance ( $G_s$ ) data shown in Fig. 2.11

Temperature (K)	300	160	30
148 nm diameter SWCN bundle	9%	14%	36%
10 nm diameter SWCN bundle	36%	57%	--

To obtain the thermal conductivity, the length and diameter of the sample need to be measured. SEM was used to measure the length of the sample. The uncertainty of the SEM measurement is about 10 nm. Thus, for a 2- $\mu\text{m}$ -long sample,  $\delta L/L = 0.5\%$ . To obtain the diameter, a tapping mode atomic force microscope was used to measure the sample segment that is located on top of the Pt electrode. The uncertainty of the diameter measurement was about 0.3 nm. For the 10 nm- (or 148 nm-) diameter SWCN bundle, this introduces an additional uncertainty of 6% (or 0.4%) to the calculated thermal conductivity. These uncertainty values are usually smaller than that introduced by the uncertainty of  $G_s$ . However, the calculated thermal conductivity ( $k$ ) does not take into account of the contact thermal resistance ( $G_c$ ), and thus represents a lower bound of  $k$ .

## **2.4 MEASUREMENT RESULTS AND DISCUSSION**

Figure 2.11 show the measurement results of thermal conductivity of a 148-nm- and a 10-nm-diameter SWCN bundles and an individual SWCN grown by the CVD method with a diameter in the range of 1~3 nm. The accurate diameter of the individual SWCN needs to be measured using TEM. As a comparison, previous measurement result of an individual multiwall (MW) CN is shown in the same figure. The measured thermal conductivity of the individual SWCN is higher than that of the MWCN and those of the two SWCN bundles, because inter-shell and inter-tube phonon scattering is absent in the individual



SWCN. For the 148-nm-diameter SWCN bundle, the peak thermal conductance occurs at about 310 K. This indicates that at this temperature, Umklapp phonon-phonon scattering starts to dominate over defect and boundary scattering of phonons. For the mat sample used in the work by Hone *et al.* (1998), defect and boundary scatterings dominate phonon transport up to 350 K. The discrepancy between two measurements suggests that the phonon mean free path due to defect and boundary scattering is longer for the bundle in this work than for the mat. At low temperatures in the range of 14.5~50 K, the thermal conductance of the 148-nm-diameter SWCNT bundle exhibits a  $T^{1.5}$  dependence. This is different from the quadratic temperature dependence observed for MWCN (Kim *et al.*, 2001). Due to inter-tube phonon scattering in the bundle, however, the low temperature results do not exhibit a linear temperature dependence that is expected for individual SWCNs. The large uncertainty in the data for this CVD SWCN is caused by the uncertainty in the diameter of the sample. This uncertainty can be reduced by a careful measurement using TEM or Raman Spectroscopy.

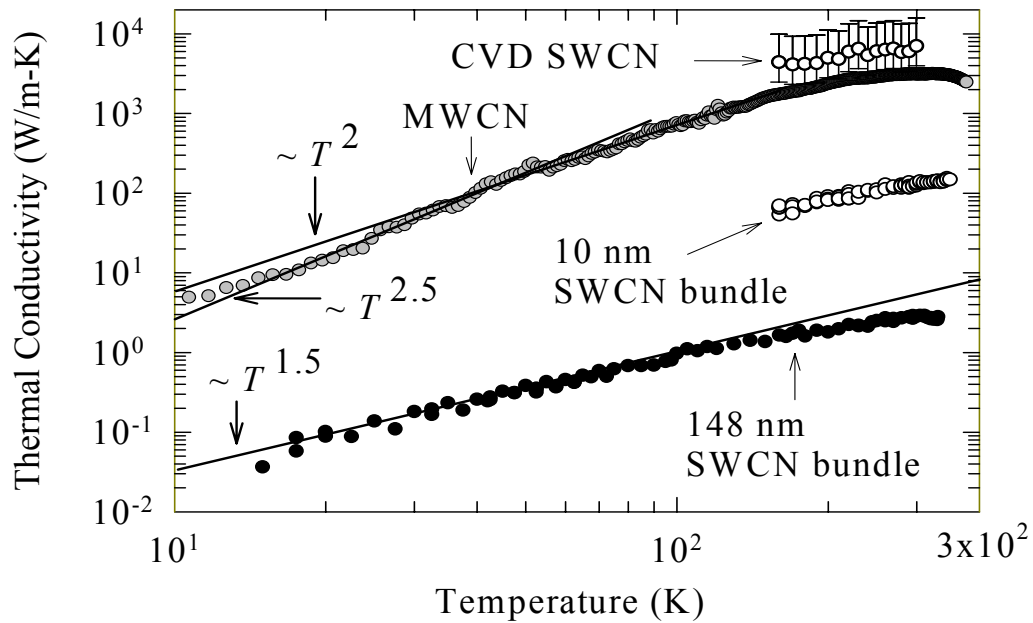


Figure 2.11: Thermal conductivities of a 1 to 3-nm-diameter individual CVD SWCN, a 10-nm- and another 148-nm-diameter SWCN bundles, and an individual MWCN in reference Kim *et al* (2001).

The electrical conductance of the CN samples was also measured using the microdevice, as shown in Fig. 2.12. For the 10-nm-diameter bundle, the electrical conductivity shows a power law dependence of  $T^{1.7}$  with temperature. For the 148-nm-diameter bundle, the electrical conductance shows a different dependence ( $T^{1.5}$ ) for temperatures below 60 K. Above 60 K, a linear  $T$  dependence can be observed for this sample. This behavior is different from the results obtained by Bockrath *et al.* (1999) and Yao *et al.* (1999), where a single

$T^{0.6}$  dependence was observed for smaller metallic SWCN bundles in the range of 4-400 K. The  $T^{0.6}$  behavior was thought to be caused by the tunneling resistance from the metal electrodes to the nanotube according to the Luttinger-Liquid model (Bockrath *et al.*, 1999). For the relatively larger bundle in this work, electron scattering in the bundle is likely to be significant, giving rise to a more complicated behavior.

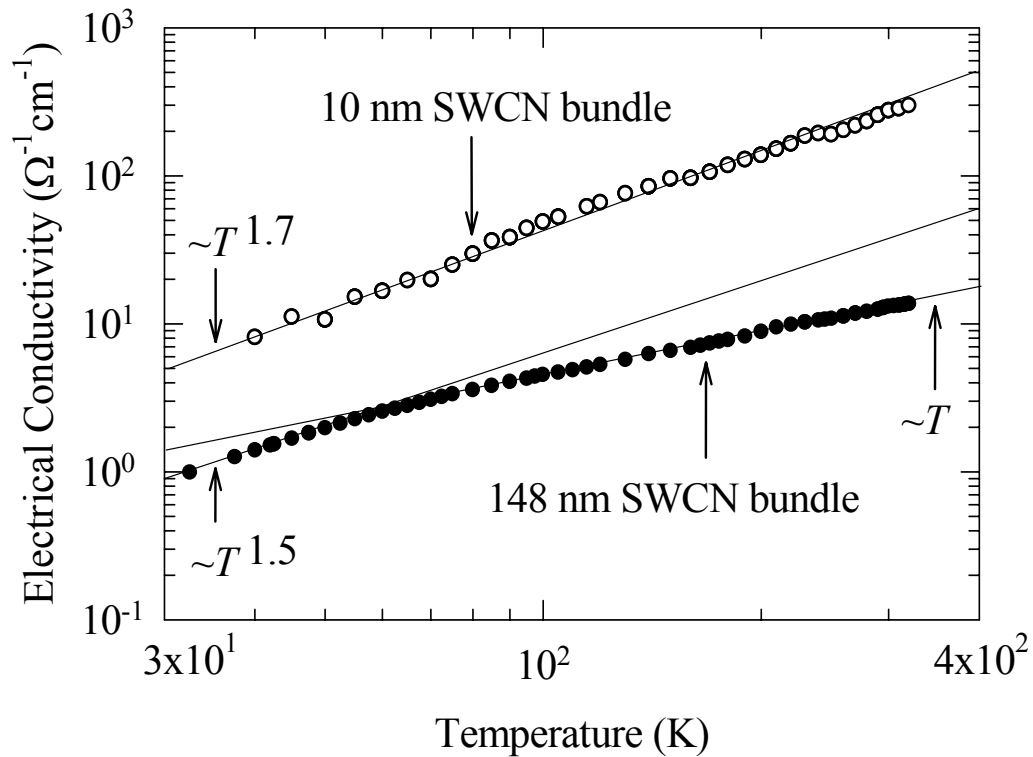


Figure 2.12: Measured electrical conductivity of a 148-nm- and a 10-nm-diameter SWCN bundle.

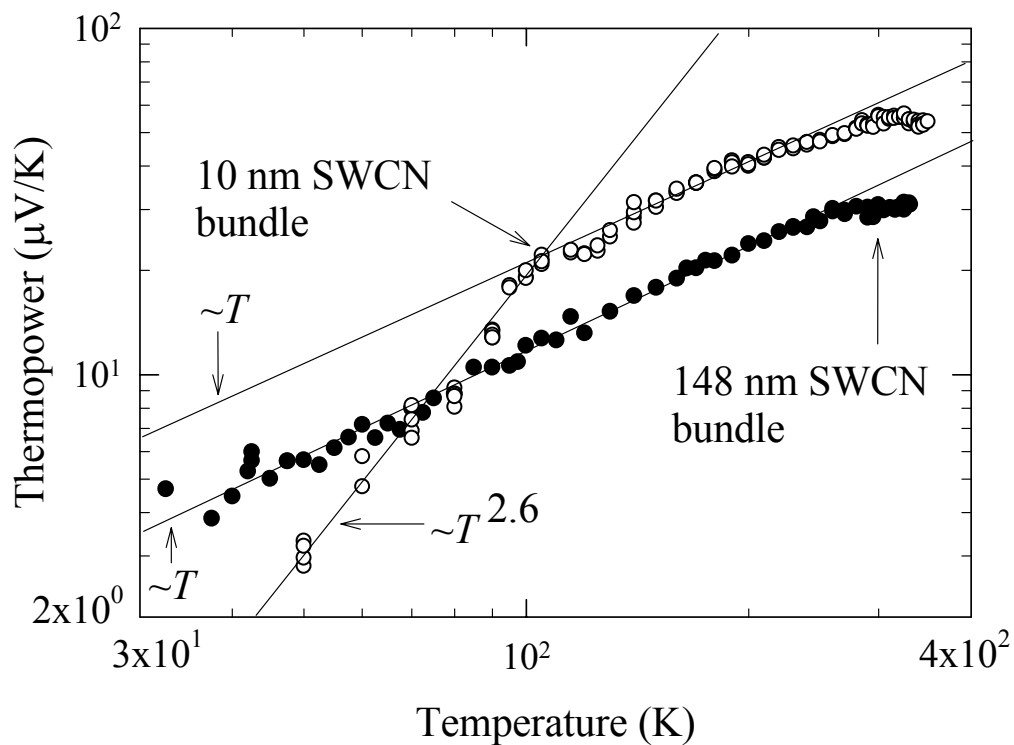


Figure 2.13: The thermopower of an individual SWCN and two SWCN bundles as a function of temperature.

As discovered by Collins *et al.* (2000), the electrical conductance and Seebeck coefficient of SWCN bundles are very sensitive to oxygen exposure. Oxygen doping can result in enhanced electrical conductance of semiconducting SWCNs and hole-type majority carriers of a bundle, which usually consists of both metallic and semiconducting SWCNs. The hole-doping further results in positive values of Seebeck coefficient that is much larger than that of a simple

metal. As SWCN bundles were deoxygenated in high vacuum ( $10^{-6}$  to  $10^{-8}$  Torr), negative values of Seebeck coefficient with smaller magnitudes than those of oxygenated samples were found (Collins *et al.*, 2000 and Bradley *et al.*, 2000).

Because a large positive Seebeck coefficient was observed in the measurement, it is very likely that the two SWCN bundles in the measurements were still oxygen doped, although they were kept in vacuum for a few hours before the measurement. Additionally, the measured Seebeck coefficient of the two bundles depends linearly on temperature for most of the temperature range. The linear behavior represents that of the diffusion thermopower of a metallic system. For the 10-nm-diameter bundle, deviation from the linear behavior is observed for temperatures below 90 K. The deviation could be caused by the suppression of the phonon-drag contribution on thermopower (Scarola and Mahan, 2002). From these measurement results, the thermoelectric figure of merit, i.e.  $ZT \equiv S^2T/RG$  was calculated. As shown in Fig. 2.14, the  $ZT$  value is rather small for the two SWCN bundles.

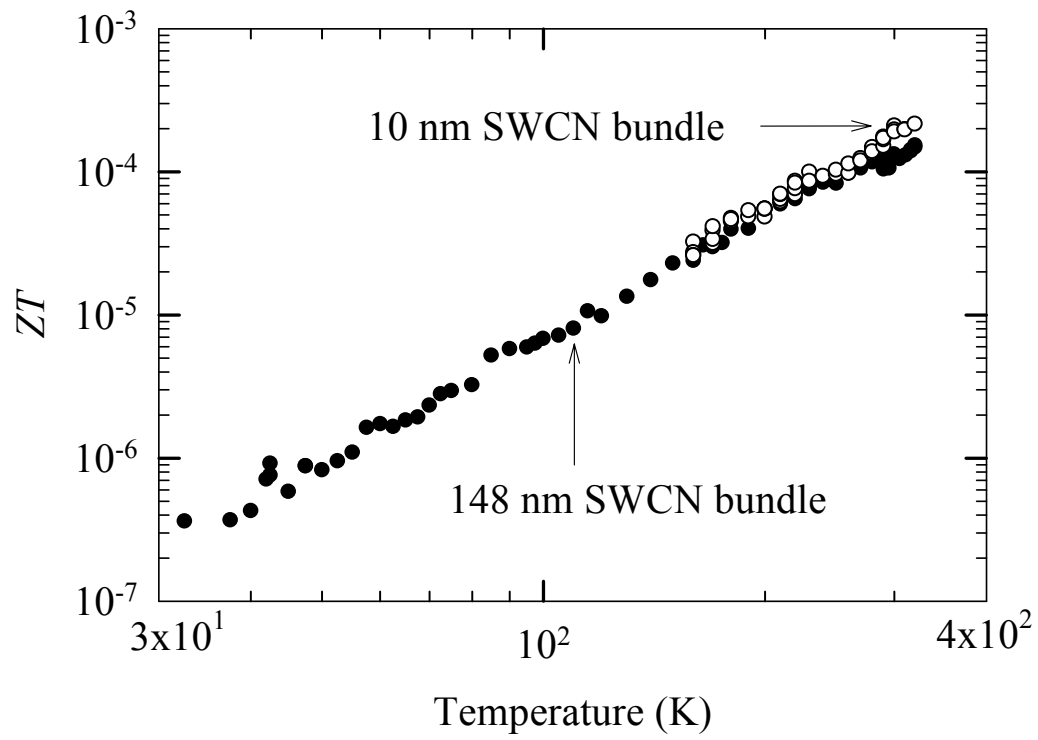


Figure 2.14: Thermoelectric figure of merit ( $ZT$ ) of a 148-nm- and a 10-nm-diameter SWCN bundle.

## Chapter 3: Integration of Nanobelts with Microsystems for Chemical Sensing

The microdevice for thermophysical property measurements was also used for gas sensor applications. As shown in Fig. 2.1 and described in section 2.1, the device consists of two adjacent silicon nitride ( $\text{SiN}_x$ ) membranes supported by long  $\text{SiN}_x$  beams. A serpentine PRT is patterned on each membrane. Two separate parallel Pt electrodes are patterned on the two membranes, forming an electrode pair for trapping metal oxide nanobelts. The device is used to raise the temperature of the nanobelts so as to enhance the sensitivity.

In air, oxygen molecules adsorbed on metal oxide surface deplete free charge carriers thereby reducing electrical conductivity of the metal oxide. For  $\text{SnO}_2$  of a rutile structure, oxygen atoms bridged to tin atoms are missing on the surface. This induces dipole layers, which result in electron affinity that attracts molecules in environment.

To release free charge carriers trapped on the surface, the PRT of the microdevice was Joule-heated to increase the temperature of the nanobelt. In addition, at high temperature, less reactive oxygen surface ions ( $\text{O}_2^-$ ) adsorbed on the surface are transformed into more reactive forms  $\text{O}^-$ ,  $\text{O}^{2-}$  ions (Ding, 2001, Anothainart, 2003, and Lantto, 2001). Hence, the electrical conductance of the

metal oxide can be increased by the thermal activation and the enhanced desorption of oxygen ions from its surface.

### **3.1 EXPERIMENTAL SETUP**

#### **3.1.1 Sample preparation**

Nanobelts can be trapped on the Pt electrode pair using three different approaches. In the first one, a solution containing the nanobelts is dropped on a wafer that contains a large number of densely-packed membrane structures. It was found that nanobelts were often adsorbed on the Pt electrodes after the solution was spun off, as described in section 2.2.

To increase the assembly yield, an electric field-directed assembly method has been investigated. In this method, the two Pt electrodes in the MEMS device are connected to an AC voltage source. As a solution containing the nanobelts is dispersed on the surface of the MEMS array, the frequency of the AC field can be adjusted to generate an attractive force on the nanobelts, which are polarized in the electric field. This phenomenon is called positive dielectrophoresis (Pohl, 1978), where a polarizable particle in a nonuniform AC electric field is attracted to regions of high field strength. A more detailed description of dielectrophoresis can be found in section 4.1. The attractive or positive dielectrophoretic force can be used to align and trap a nanobelt onto the two Pt electrodes. The suitable frequency and root-mean-square (rms) amplitude of the AC voltage have been



found to be about 1 MHz and 5 V, respectively, for trapping the nanobelt dispersed in Isopropyl alcohol (IPA). Similar methods have been reported for trapping nanowires (Chen, 2001 and Smith, 2000) and nanotubes (Duan, 2001) with a yield approaching 100%.

Figure 3.1 shows a SnO<sub>2</sub> nanobelt trapped on the two Pt electrodes of the MEMS device. Pt was deposited on the contact of the nanobelt using FIB to improve the electrical conductance and to prevent gas species from poisoning the contact.

### **3.1.2 Characterization of the microdevice for sensor applications**

As described in the previous section, the sensor temperature needs to be raised up to 400°C by Joule-heating of the PRTs. Because of the large thermal resistance in the long and low-thermal conductivity SiN<sub>x</sub> beams, the membrane is thermally isolated from the substrate (see Fig. 2.1). Hence, the device only consumed 2.2 mW for raising the membrane temperature to 400°C, as shown in Fig. 3.2. The temperature rise shown in Fig. 3.2 was measured with the use of the PRT.

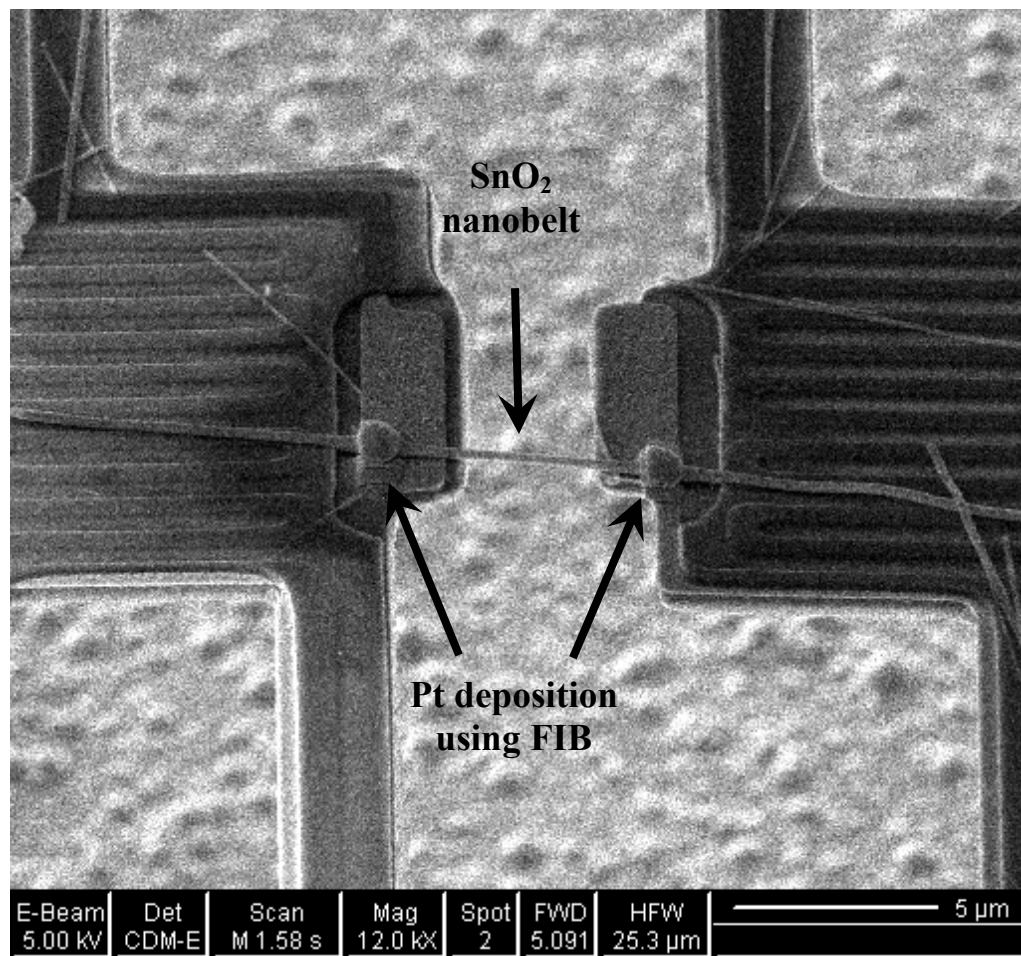


Figure 3.1: SEM of a SnO<sub>2</sub> nanobelt assembled on two Pt electrodes of a suspended MEMS device, which was used for thermophysical property measurements of nanostructures. To enhance electrical conductivity and prevent poisoning effect, Pt was deposited on the two contacts using FIB.

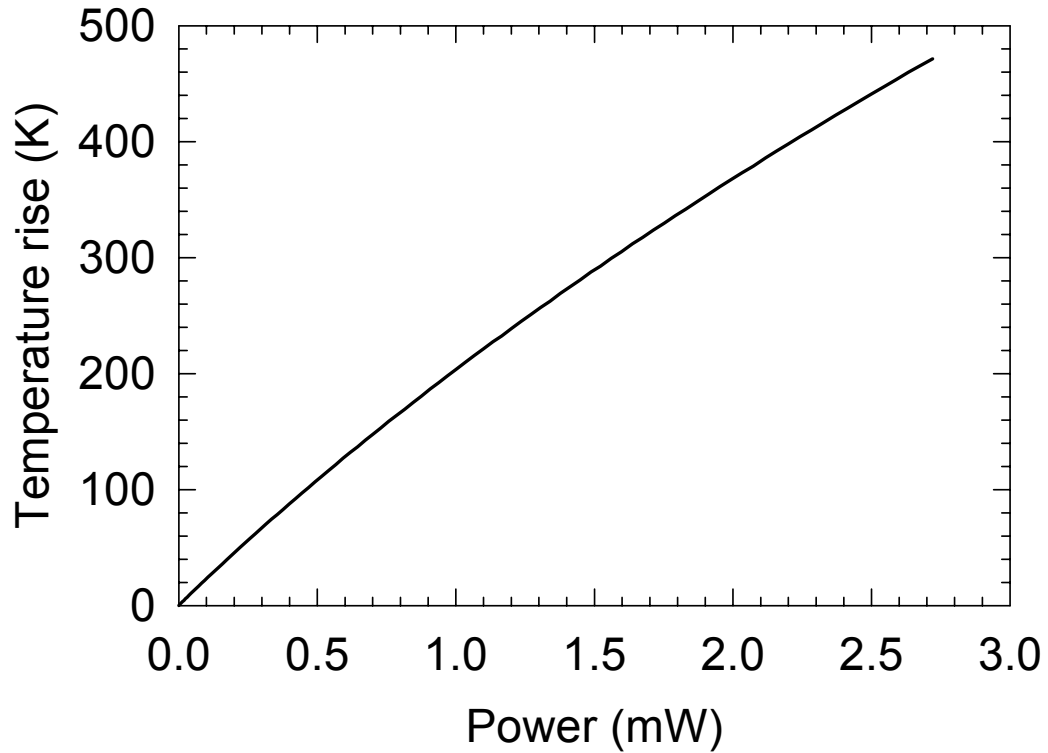


Figure 3.2: Temperature rise of the suspended membrane as a function of power consumption of the Pt heater line.

To calculate the temperature of the membrane, the voltage drop ( $V$ ) in the PRT was measured as the DC heating current ( $I$ ) was slowly ramped up to a value in the range of 4-10  $\mu\text{A}$  (see Fig. 2.7). The differential resistance  $R_h$  of the heating PRT was obtained by the following method. For a slow voltage ramp rate (i.e.,  $I \approx$  constant), the voltage drop in the heater is measured and can be written as

$$V_{PRT} = IR_h(I) = I \{R_h(I=0) + (dR_h/dT) \Delta T_h\} \quad (3.1)$$

Because all the heat generated in the heater and legs are conducted through the ten beams, it can be shown that

$$2G_b \Delta T_h = I^2 (R_h + R_L) \quad (3.2)$$

From Eq. 3.1 and Eq. 3.2, one can write that

$$V_{PRT} = I \{R_h(I=0) + (dR_h/dT) I^2 (R_h + R_L) / (2G_b)\} \quad (3.3)$$

Therefore, the resistance as a function of current is

$$R_h(I) = \frac{dV_{PRT}}{dI} = R_h(I=0) + 3 \frac{dR_h}{dT} \frac{I^2 (R_h + R_L)}{2G_b} \quad (3.4)$$

Since  $\Delta T_h(I) = I^2 (R_h + R_L) / (2G_b)$ , Eq. 3.4 can be written as

$$\Delta R_h = R_h(I) - R_h(I=0) = 3 (dR_h/dT) \Delta T_h(I) \quad (3.5)$$

Therefore, the temperature rise is

$$\Delta T_h(I) = \frac{\Delta R_h(I)}{3 \frac{dR_h(I=0)}{dT}}; \Delta R_h(I) = R_h(I) - R_h(I=0) \quad (3.6)$$

where  $R_h$  is the temperature dependence of the resistance.  $dR_h/dT$  was calculated from the measured resistance at different temperatures.

The as-assembled nanobelt sensor was tested with gas species. The sensor was contained in a small flow-through chamber (sensor box). For NO<sub>2</sub> or ethanol, a cylinder, containing the gas species balanced with air, was connected to a flow meter. To vary the concentration of the gas species, room air was purged into the

mixing chamber through a flow meter, as shown in Fig. 3.3a. To test the sensor for dimethyl methylphosphonate (DMMP), a permeation tube, containing liquid phase of DMMP was used. The permeation tube was inserted in a U-shape stainless steel tubing, which was heated to evaporate the DMMP. A pump was connected to the U-shape tubing in order to purge the DMMP to the sensor box. The concentration of the gas species can be calculated from  $C=K \times P/F$ , where C, F, P, and K are concentration in ppm by volume, diluent flow rate in cc/min, permeation rate in ng/min, and molar constant ( $=24.46/\text{molecular weight}$ ), respectively. A pipe line was connected to a mixing tee to vary the concentration of the gas species, as shown in Fig. 3.3b. A DC current was supplied to the PRT to raise the temperature of the membrane. With a constant voltage applied to the nanobelt, the current in the nanobelt was recorded when the chamber was purged with a gas specie and room air, repeatedly.

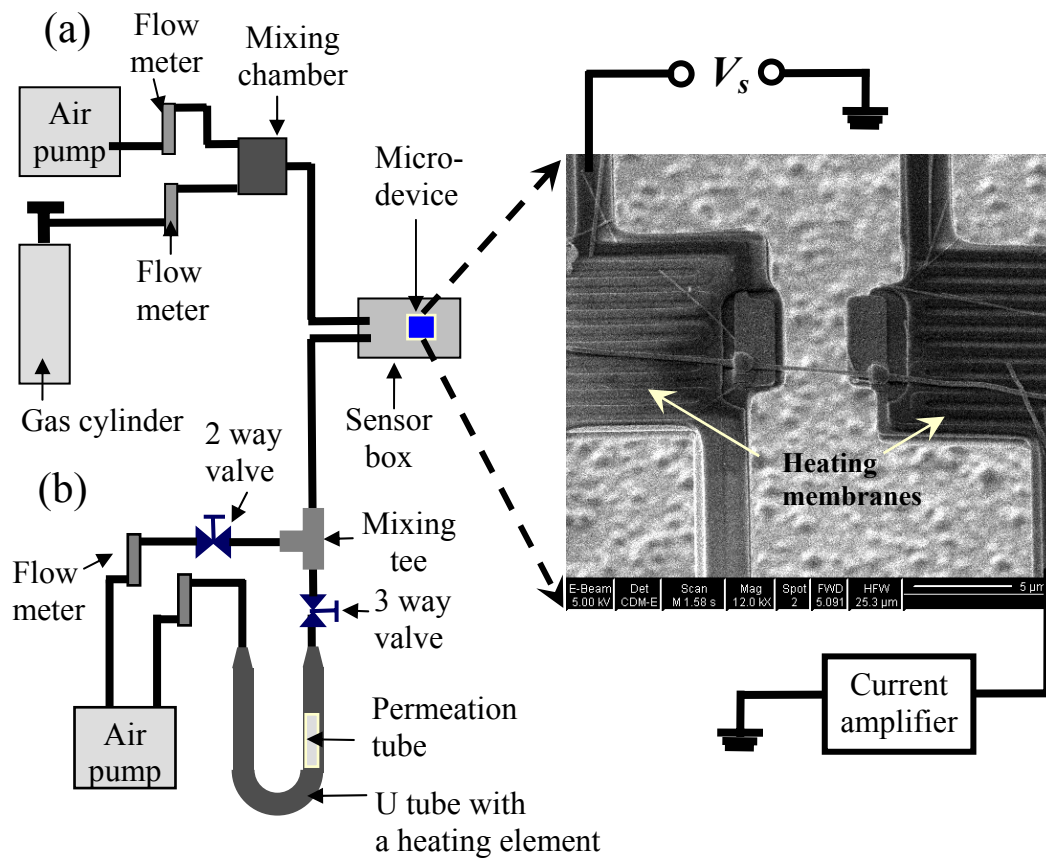


Figure 3.3: Experimental setup to test the nanobelt sensor for (a)  $\text{NO}_2$  and Ethanol gas species, (b) DMMP gas species.

### 3.2 MEASUREMENT RESULTS AND DISCUSSION

Figure 3.4 shows the sensor response to 0.2, 0.5, 0.9, 1.7, and 10 ppm NO<sub>2</sub> balanced with air when the nanobelt was Joule-heated to 200 °C. The dotted lines in the figure represent the gas concentrations that flowed to the sample chamber.

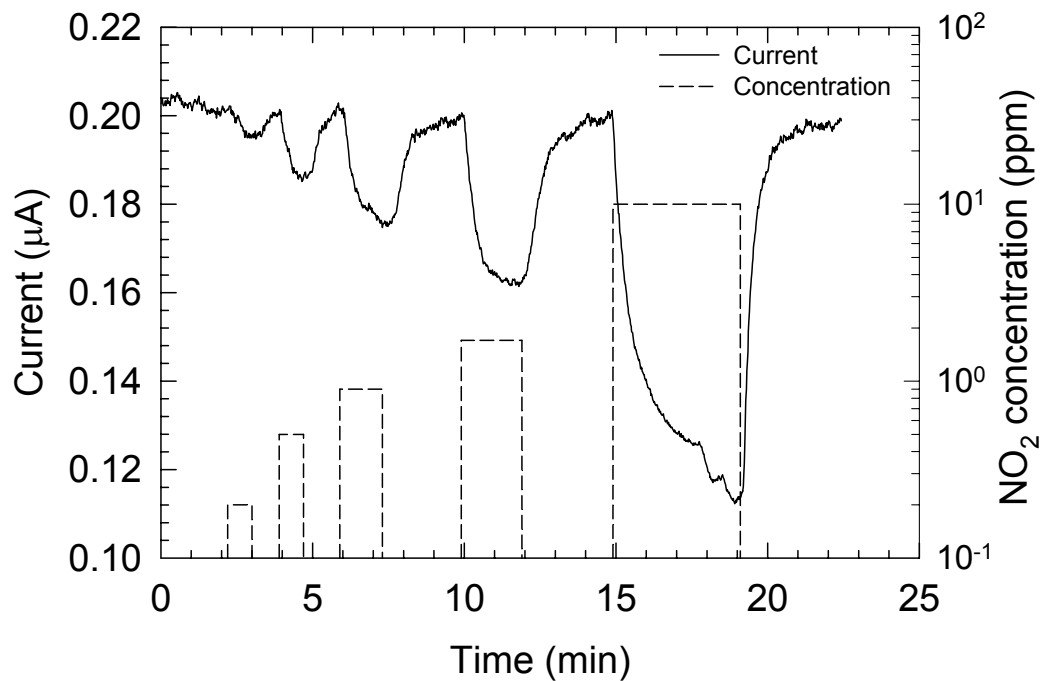


Figure 3.4: Response of the as-assembled nanobelt-MEMS sensor to 0.2, 0.5, 0.9, 1.7, and 10 ppm NO<sub>2</sub> balanced with air when the nanobelt temperature was 200 °C. The voltage applied to the nanobelt was 2 V.

As the NO<sub>2</sub> gas was introduced to the chamber, the current dropped immediately and recovered quickly after NO<sub>2</sub> gas was replaced by room air. The reduction in current increased with the NO<sub>2</sub> gas concentration, being about 45% change in current at 10 ppm concentration. More importantly, it does not show sensor-poisoning effects. As soon as the NO<sub>2</sub> gas was removed, the conductance recovered fully to its original value in only a few minutes. The nanobelt shows such high repeatability because of the absence of grain boundaries in the nanobelt.

Figure 3.5 shows the sensor response to 125, 83, 250, and 23 ppm ethanol balanced with air when the device was Joule-heated to 150 °C. While the NO<sub>2</sub> gas depletes electrons by forming NO<sup>2-</sup> on the sensor surface, OH<sup>-</sup> group in the ethanol gas desorbs oxygen ions from the nanobelt and thereby enhances electrical conductance, leading to an increase in current soon after the ethanol gas was introduced to the chamber. Figure 3.6 shows the sensor response to 78 and 53 ppb DMMP balanced with air when the device was Joule-heated to 230 °C.



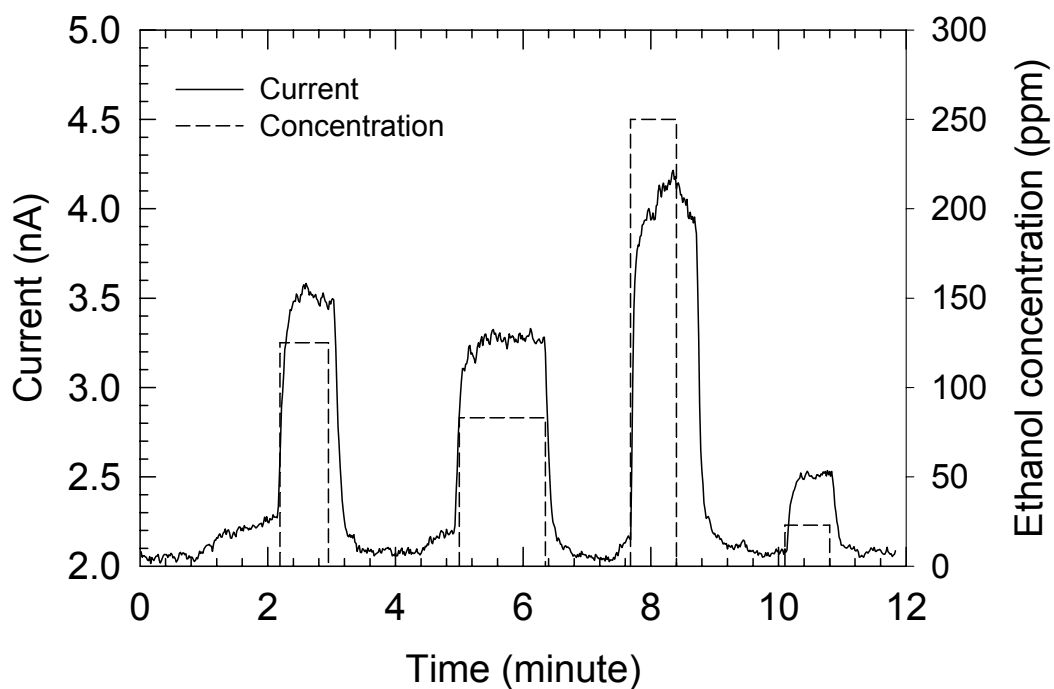


Figure 3.5: Response of the as-assembled nanobelt-MEMS sensor to 125, 83, 250, and 23 ppm ethanol balanced with air when the nanobelt temperature was 150 °C.

The voltage applied to the nanobelt was 1.0 V.

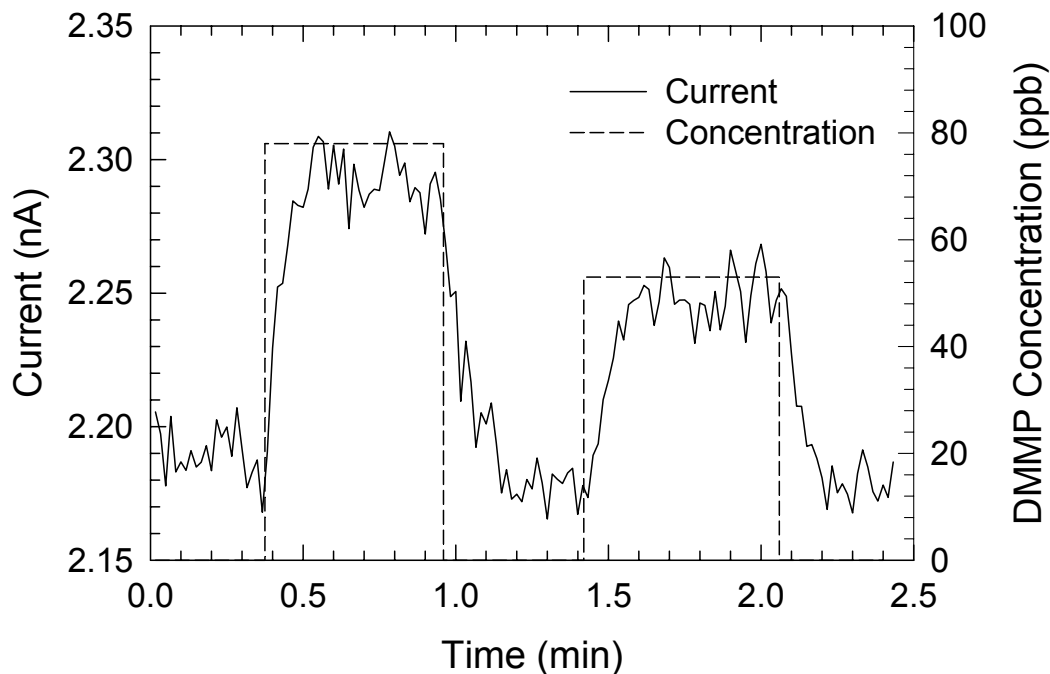


Figure 3.6: Response of the as-assembled nanobelt-MEMS sensor to 78 and 53 ppb DMMP balanced with air when the nanobelt temperature was 230 °C. The voltage applied to the nanobelt was 1.5 V.

In the aforementioned experiments, an individual single-crystalline nanobelt with Pt deposition on the contact was tested for different gas species. As shown in Fig. 3.4, 3.5, and 3.6, the sensor response was highly repeatable and fast compared with sensors based on CN films (Novak, 2003) or a bunch of nanobelts (Comini, 2002). Note that the excellent recovery could only be achieved with Pt

deposition on the contacts. Without Pt deposition, the conductance did not recover fully or quickly due to contact poisoning.

The sensitivity of the as-assembled sensor can be further enhanced by functionalizing the nanobelts with different catalytic additives or dopants (Kovacs, 1998 and Oh, 1993). The selectivity of metal oxide sensors can be obtained using a pattern recognition approach, where an array of different nanobelt sensors generates a distinct response pattern for a gas species or mixture. With the use of the electric field-directed assembly method, moreover, it is feasible to fabricate selective gas sensor arrays consisting of functionalized metal oxide nanobelts assembled into a MEMS platform that consists of a micro chromatography column (Noh, 2002) and pre-concentrator (Tian, 2003) for gas separation and pre-concentration. This directed assembly approach can thus enable one to combine nanomaterials synthesis with MEMS fabrication for the large-scale manufacturing of integrated nano-sensor systems.

## **Chapter 4: A Three-Dimensional (3D) Dielectrophoretic Particle Focusing Channel for Micro-Cytometry Applications**

The electric field manipulation technique has not only been used to assemble nanomaterials with MEMS, but also been used to focus biological cells in a microfluidic channel for cytometry applications. Flow cytometry is a powerful and versatile method of rapidly analyzing large populations of cells and other particulate or molecular analytes that have been captured on the surface of carrier particles. However, the key components of the system, hydrodynamic focusing and optical systems, make conventional cytometers complex, large, and expensive. To eliminate these drawbacks, a dielectrophoretic particle focusing technique combined with MEMS has been developed explored to replace the hydrodynamic focusing mechanism. To focus particles, microelectrodes are patterned on the circumference of the channel to generate AC fringing fields that result in negative dielectrophoretic forces directing cells from all directions to the center of the channel.

In this chapter, the design and fabrication of the micro flow cytometer are discussed. In addition, experimental results with microbeads and human leukemia cells are presented.

#### 4.1 THEORETICAL BACKGROUND

Dielectrophoresis is the translational motion of a particle in a suspending medium due to the interaction between the polarization of the particle and an applied nonuniform electric field. A dielectrophoretic force  $\vec{F}$  acting on a spherical particle of radius  $r$  subjected to an AC electric field  $\vec{E}$  of angular frequency  $\omega$  can be described as (Wang, 1994)

$$\vec{F} = 2\pi\epsilon_m r^3 \text{Re}[f(\epsilon_p^*, \epsilon_m^*)] \nabla \vec{E}_{rms}^2 \quad (4.1)$$

The subscripts  $m$ ,  $p$ , and  $rms$  stand for medium, particle, and root-mean-square value, respectively. The term  $\epsilon_i^*$  is the complex permittivity of the indexed material, which is defined as

$$\epsilon_i^* = \epsilon_i - j\sigma_i / \omega \quad (4.2)$$

where  $\epsilon$  and  $\sigma$  are permittivity and conductivity of a particle or medium, and  $j = \sqrt{-1}$ . For a spherical homogeneous particle with ohmic loss, the expression  $f(\epsilon_p^*, \epsilon_m^*)$ , referred as the Clausius-Mossotti factor, can be defined as

$$f(\epsilon_p^*, \epsilon_m^*) = \frac{\epsilon_p^* - \epsilon_m^*}{\epsilon_p^* + 2\epsilon_m^*} = \frac{\epsilon_p - \epsilon_m - j(\sigma_p - \sigma_m) / \omega}{\epsilon_p + 2\epsilon_m - j(\sigma_p + 2\sigma_m) / \omega} \quad (4.3)$$

At frequencies well above and below  $\tau_{MW}^{-1} = (\sigma_p + 2\sigma_m) / (\epsilon_p + \epsilon_m)$ , the real component of the Clausius-Mossotti factor becomes independent of the frequency of the electric field (Jones, 1995), i.e.

$$\text{Re}[f(\varepsilon_p^*, \varepsilon_m^*)] \rightarrow \begin{cases} \frac{\sigma_p - \sigma_m}{\sigma_p + 2\sigma_m}, & \text{for } \omega\tau_{MW} \ll 1 \\ \frac{\varepsilon_p - \varepsilon_m}{\varepsilon_p + 2\varepsilon_m}, & \text{for } \omega\tau_{MW} \gg 1 \end{cases} \quad (4.4)$$

On the other hand, the Clausius-Mossotti factor for a heterogeneous particle, such as a biological cell, deviates from Eq. 4.3 due to the different polarizability of the particle. For instance, eukaryotic cells, which contain nucleus and other organelles suspended in a semifluid medium called the cytosol, are enclosed by outer membranes. Those layered spherical particles can be modeled using an effective complex permittivity. For the particle that has a single outer shell of thickness  $d$ , the complex permittivity of the particle in Eq. 4.3 can be substituted by the effective complex permittivity described as (Jones, 1995)

$$\varepsilon_{p,eff}^* = \varepsilon_s^* \left[ \frac{\left( \frac{r}{r-d} \right)^3 + 2 \left( \frac{\varepsilon_{int}^* - \varepsilon_s^*}{\varepsilon_{int}^* + 2\varepsilon_s^*} \right)}{\left( \frac{r}{r-d} \right)^3 - \left( \frac{\varepsilon_{int}^* - \varepsilon_s^*}{\varepsilon_{int}^* + 2\varepsilon_s^*} \right)} \right] \quad (4.5)$$

where  $\varepsilon_s^*$  and  $\varepsilon_{int}^*$  are the complex permittivity of the shell and that of the cell interior, respectively. In the case of  $d \ll r$ , which holds for most of cells that lack a cell wall such as mammalian cells, we can rewrite  $\varepsilon_s^*$  in Eq. 4.5 using the following relation

$$\varepsilon_s^* = C_s^* d = \left( C_s - \frac{jG_s}{\omega} \right) d \quad (4.6)$$

where  $C_s^*$ ,  $C_s$ , and  $G_s$  are the complex specific capacitance, specific capacitance, and specific conductance of the shell, respectively.

#### 4.2 POSITIVE AND NEGATIVE DIELECTROPHORESIS

As shown in Eq. 4.1, the dielectrophoretic force is affected by the properties of the particle and the medium as well as the amplitude of the applied electric field. The force is attractive or repulsive depending on the sign of the real part of the Clausius-Mossotti factor, which is a function of the frequency of the electric field as well as the dielectric properties of the particle and the suspending medium.

When  $\text{Re}[f(\varepsilon_p^*, \varepsilon_m^*)] > 0$  (or  $< 0$ ), particles under the dielectrophoretic force are attracted to (or repelled from) regions of high electric field strength, the phenomenon is respectively called positive or negative dielectrophoresis (Pohl, 1978 and Jones, 1995). Figure 4.1 shows the dielectrophoretic force acting on particles in a nonuniform electric field in two-dimensional (2D) space.

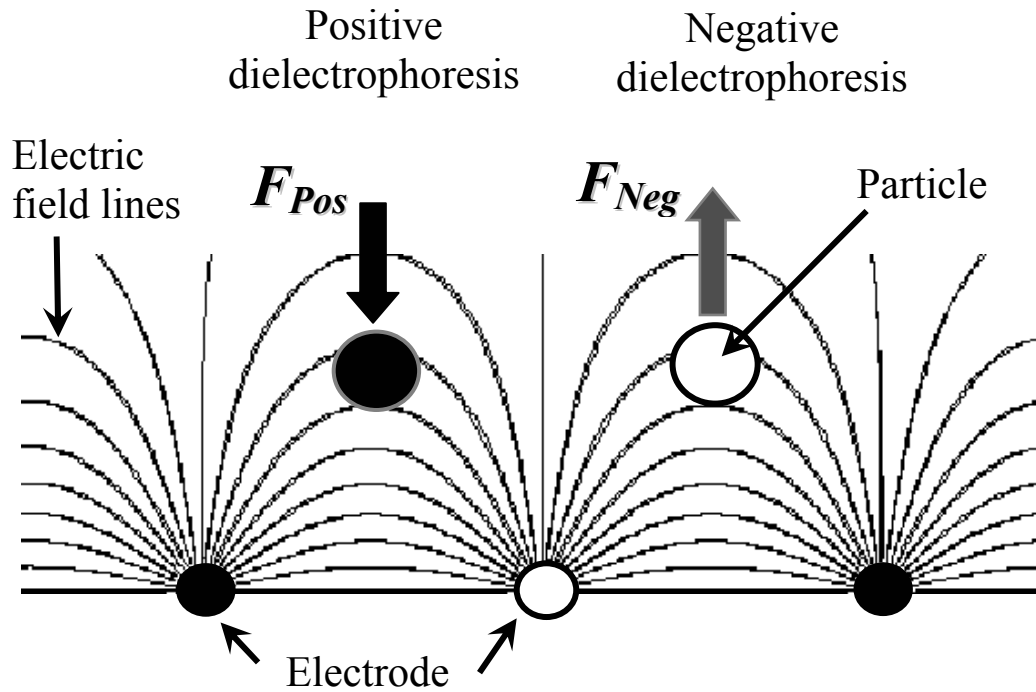


Figure 4.1: A schematic diagram showing the positive and negative dielectrophoretic forces exerted on particles in a nonuniform electric field created by applying voltage to the electrodes (positive voltage: filled electrodes, ground: hollow electrode)

At the so-called crossover frequency,  $\text{Re}[f(\varepsilon_p^*, \varepsilon_m^*)] = 0$  and thereby the dielectrophoretic force acting on the particle is zero. At frequencies above the crossover frequency,  $\text{Re}[f(\varepsilon_p^*, \varepsilon_m^*)]$  is positive for mammalian cells with a maximum value of 1, whereas at frequencies below the crossover frequency,



$\text{Re}[f(\varepsilon_p^*, \varepsilon_m^*)]$  has a minimum value of -0.5. The dielectric properties of the particle are affected by several factors including the particle type, membrane structure, internal organization, and, in the case of cells, viability. In order to achieve the optimum dielectrophoretic focusing of particles regardless of the particle type and structure, one needs to operate the microcytometer in a regime where the repulsive dielectrophoretic force is maximized. This can be achieved by using a frequency well below the crossover value and a voltage just below the maximum that doesn't damage the cells. Although the medium properties can be modulated to obtain appropriate value of the Clausius-Mossotti factor, it is inconvenient to change medium properties frequently during the operation of the microcytometer. Consequently, only the applied voltage was varied in the experiment.

To estimate the frequency range for negative dielectrophoretic particle focusing, the homogeneous particle model and the thin shell model have been used to calculate the Clausius-Mossotti factor for a latex bead and a biological cell, respectively. Figure 4.2 shows the factor as a function of the frequency of the applied electric field for different dielectric properties of a latex bead and the surrounding medium. The permittivities of the bead and the medium used in the calculation were  $2.5\varepsilon_0$  and  $80\varepsilon_0$ , where  $\varepsilon_0$  is the permittivity of free space. The conductivity of the latex beads can be calculated as  $\sigma_p = \sigma_{p,bulk} + 2K_s / r$ , where

$\sigma_{p,bulk}$  and  $K_s$  are the bulk conductivity and surface conductance of the latex bead.

The bulk conductivity is approximately zero and the typical value of the  $K_s$  is on the order of 1 nS (Arnold, 1987 and Morgan, 1999). The Clausius-Mossotti factor is negative regardless of the frequency (case a in Fig. 4.2) unless the medium conductivity is much lower than the typical value used for cytometry applications (case c in Fig. 4.2).

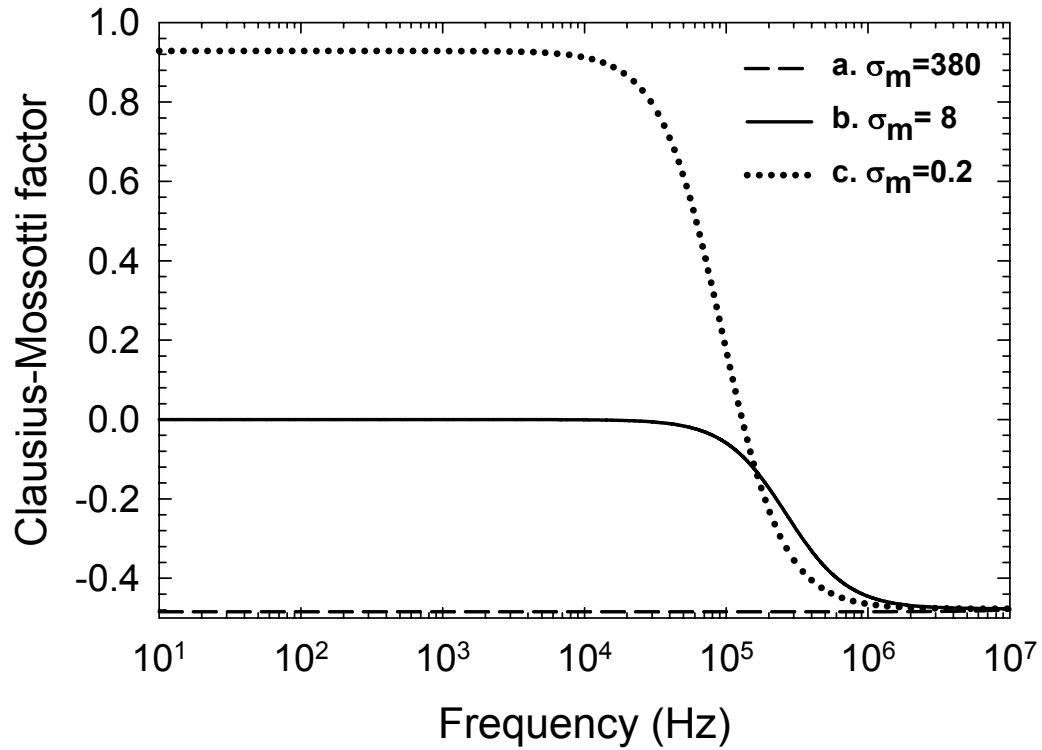


Figure 4.2: The real part of the Clausius-Mossotti factor for a 10- $\mu\text{m}$ -diameter latex bead as a function of the frequency of the applied voltage for the different dielectric properties of the medium and the bead. The permittivity and conductivity of the bead are  $2.5\epsilon_0$  and  $8 \mu\text{S/cm}$ , respectively. The unit of the conductivity ( $\sigma$ ) is  $\mu\text{S/cm}$  in the legend.

Figure 4.3 shows the Clausius-Mossotti factor as a function of the frequency of the applied voltage for different dielectric properties of a biological cell. The membrane dielectric properties of the HL-60 leukemia cells (Wang, 2002) and the typical dielectric properties of the interior of a blood cell (Yang, 1999) were used for the calculation of case a in Fig. 4.3. Within the typical range of the dielectric parameters of biological cells (Gascoyne, 1995), negative dielectrophoresis could be achieved at frequencies below about 100 kHz. At high frequencies above 100 kHz, the dielectrophoretic force is determined by the frequency-dependent complex permittivities, and thus strongly depends on the frequency. At low frequencies, on the other hand, the conductivities dominate the Clausius-Mossotti factor. In a living cell, the conductivity of the plasma membrane is several orders of magnitude smaller than that of the cell interior (Gascoyne, 1997), while the conductivity of the medium can be adjusted to be of the same order as or one order smaller than that of the cell interior. Consequently, the large difference between the conductivity of the membrane and that of the suspending medium can result in the maximum negative value of the Clausius-Mossotti factor. Hence, a large negative force weakly depending on the frequency can be expected at frequencies below 100 kHz, unless the membrane conductance is assumed to be much higher than the range of 20~2000 S/m<sup>2</sup> of a typical biological cell (Gascoyne, 1995), as in case b of Fig. 4.3. Hence, this analysis

suggests that most cells can be focused by using a frequency below about 100 kHz to obtain negative dielectrophoresis. Nevertheless, a very low frequency close to DC needs to be avoided in order to prevent hydrolysis of the medium.

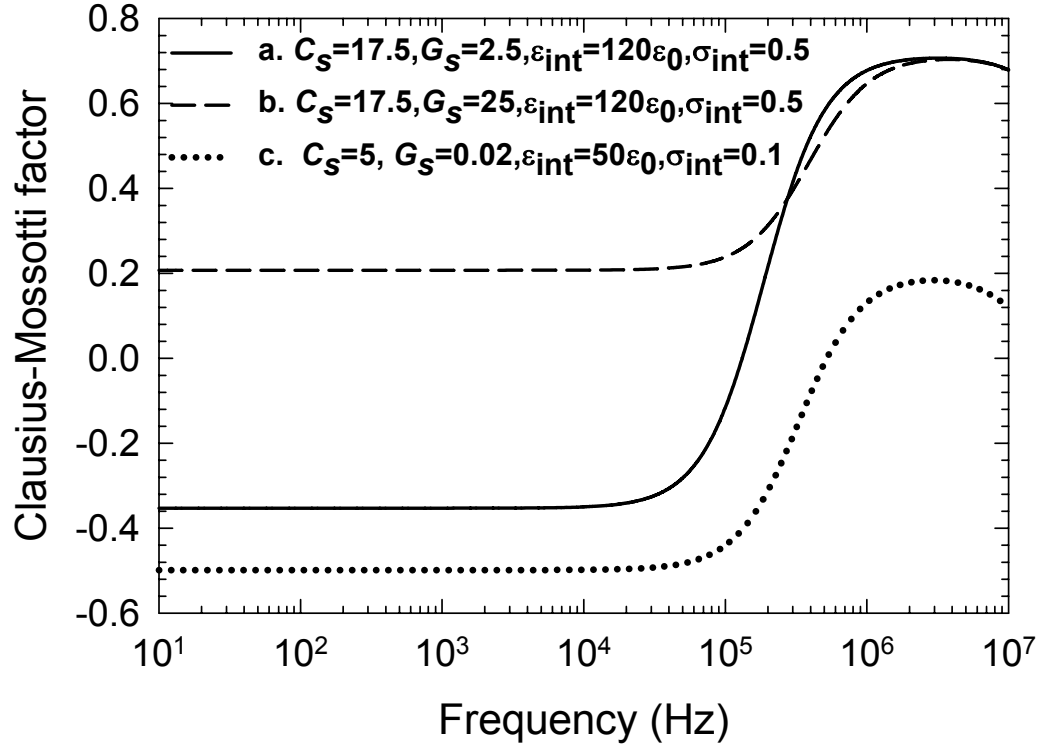


Figure 4.3: The real part of the Clausius-Mossotti factor as a function of the frequency of the applied voltage for different dielectric properties of a 10- $\mu\text{m}$ -diameter biological cell.  $\epsilon_{\text{int}}$  and  $\sigma_{\text{int}}$  are the permittivity and the electrical conductivity of the cell interior, respectively. The unit for  $C_s$ ,  $G_s$ , and  $\sigma_{\text{int}}$  in the legend are  $\text{mF}/\text{m}^2$ ,  $\text{kS}/\text{m}^2$ , and  $\text{S}/\text{m}$ , respectively. The thickness of the membrane is 5 nm. The permittivity and conductivity of the medium are  $80\epsilon_0$  and  $0.056 \text{ S}/\text{m}$ , respectively.

### **4.3 DESIGN AND FABRICATION**

#### **4.3.1 Design of dielectrophoretic particle focusing channel**

The design employs a repulsive dielectrophoretic force to focus cells to the center of a microchannel, obviating the need for fluidics beyond a simple flow to transport the particle suspension through the device. The hydrodynamic focusing system is replaced with electrode arrays to generate negative dielectrophoretic forces that drive cells to the region of the minimum field gradient. The electrode arrays are fabricated on the circumference of an elliptic-like microchannel, as shown in Fig. 4.4. In this configuration, the electric field strength gradually changes in the radial direction of the channel with the region of the minimum field gradient at the center of the channel. Hence, the resulting dielectrophoretic forces direct cells from all directions to the center of the channel.

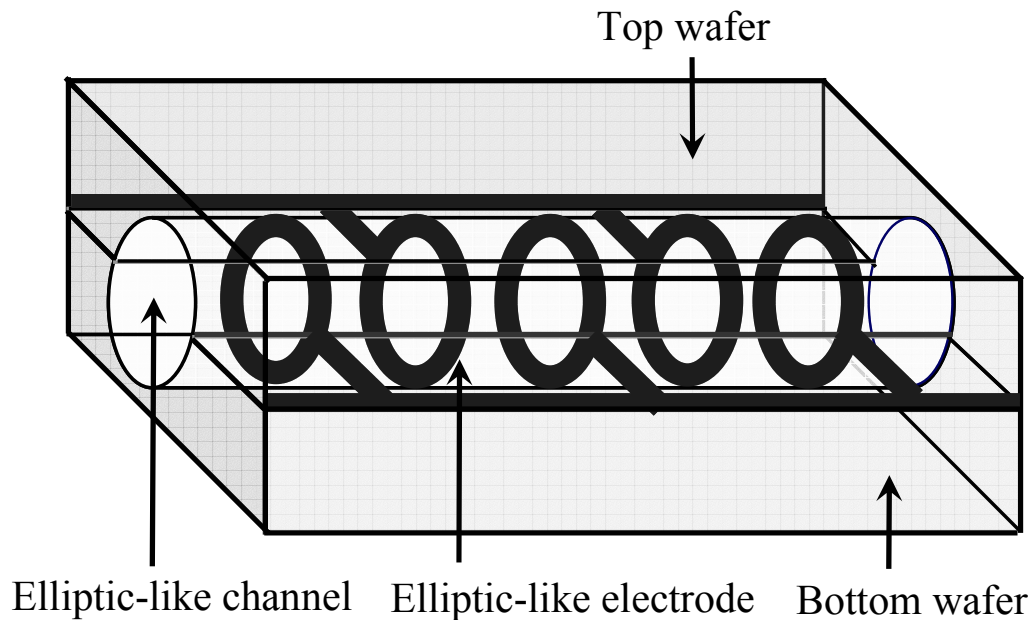


Figure 4.4: A schematic diagram of a microfluidic channel with a microelectrode array patterned on its circumference for dielectrophoretic particle focusing

A commercial simulation package (Maxwell-2D, Ansoft Corp.) has been used to calculate the electric field in a circular channel with electrode arrays fabricated on the circumference. In the calculation, a DC voltage of 7.5 V was applied to one of the two sets of the interdigitated electrodes while the adjacent set is grounded. Figure 4.5a shows the magnitude of the electric field ( $E$ ) in an R-Z cross section along the longitudinal direction of the 100- $\mu\text{m}$ -diameter channel. Figure 4.5b shows the  $-\nabla E^2$  vector field. Since the dielectrophoretic force is proportional to the product of the Clausius-Mossotti factor and  $\nabla E^2$  as described



in Eq. 4.1, the force is parallel to the direction of the  $-\nabla E^2$  vector field and directed to the center of the channel when the real part of the Clausius-Mossotti factor is negative. The minima of the magnitude of  $\nabla E^2$  are found to be at the center of the channel, where particles are focused by negative dielectrophoresis.

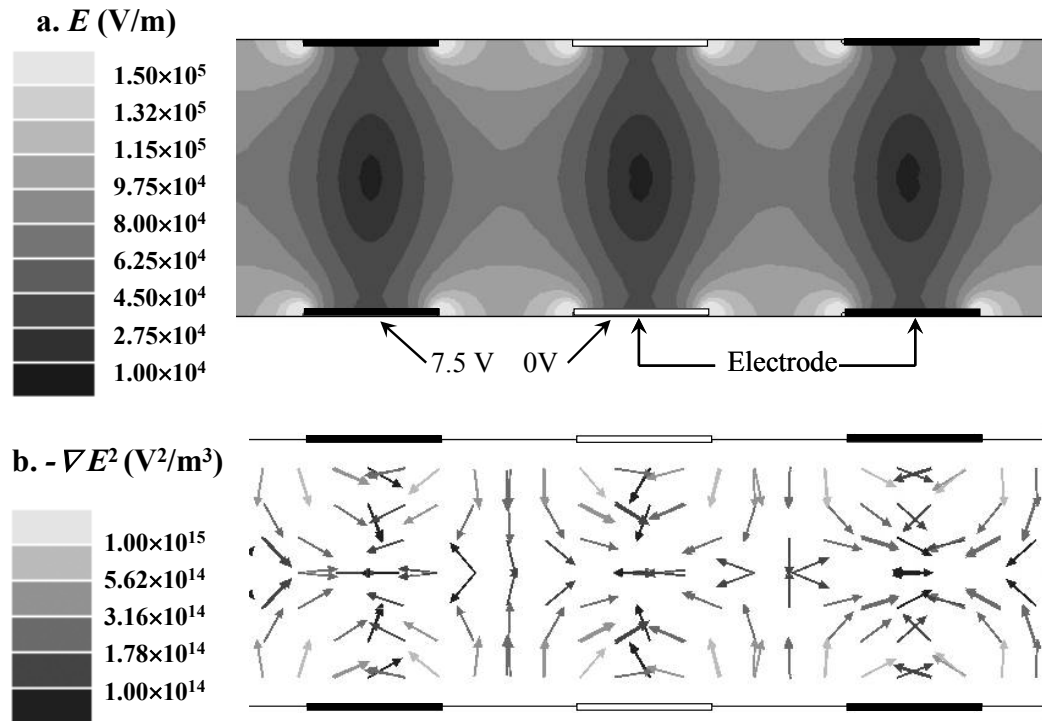
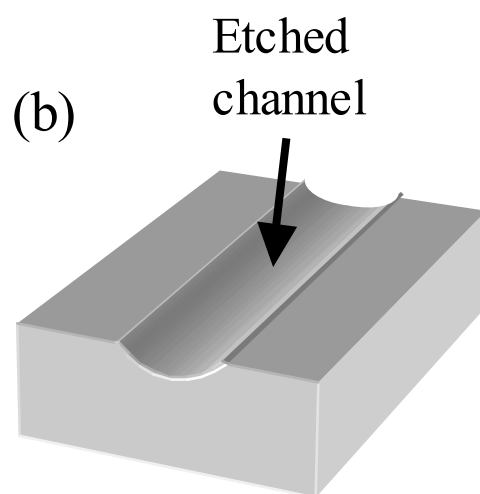
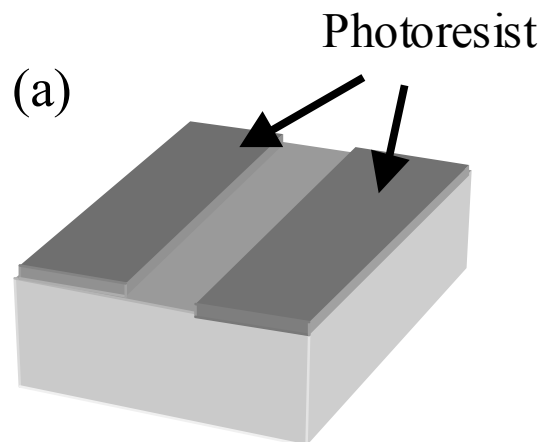


Figure 4.5: (a) Simulation results of the magnitude of the electric field ( $E$ ) in a R-Z cross section of the 100- $\mu\text{m}$ -diameter channel when a voltage of 7.5 V is applied to the black electrodes and the white electrodes are grounded. The permittivity and conductivity of the fluid in the channel are  $80 \epsilon_0$  and 560  $\mu\text{m}/\text{cm}$ . The field strength is represented by the gray scale bar. (b) The  $-\nabla E^2$  vector field. The magnitude of  $-\nabla E^2$  is represented by the gray scale bar.

### 4.3.2 Fabrication of the dielectrophoretic particle focusing channel

The microcylinders were fabricated using 500- $\mu\text{m}$ -thick, 100-mm-diameter soda lime glass wafers. The fabrication process is shown in Fig. 4.6. Because the etching of deep channels requires considerable time during which a photoresist layer may peel off from the wafer, three steps were performed to improve the adhesion of the photoresist layer. First, the wafers were cleaned in a piranha solution (37 %  $\text{H}_2\text{O}_2$ : 96 %  $\text{H}_2\text{SO}_4$  = 1:2 by volume) for 10 minutes and then immersed in a diluted HF solution ( $\text{H}_2\text{O}$ : HF = 200:1 by volume) for 30 seconds. Next, a hexamethyldisilazane (HMDS) layer was vapor-coated onto the wafers for 5 minutes to promote the adhesion of a photoresist layer. A thick AZ 9260 photoresist was then applied to avoid the formation of pinholes in the photoresist during the etching process. To obtain a uniform thickness of the photoresist layer, the photoresist was spun on the wafers at an increasing speed from 0 to 1200 rpm for 30 seconds and subsequently at 2000 rpm for 20 seconds, resulting in an 11- $\mu\text{m}$ -thick photoresist film. The wafer was left in air at room temperature for 20 minutes before undergoing a soft-baking process on a 90 °C hot plate for 15 minutes. The photoresist was patterned with a mask aligner using an exposure dose of 32-mJ/cm<sup>2</sup>, and subsequently developed in AZ 300 MIF developer for 11 minutes. To minimize stress in the photoresist, a two-stage hard-baking process was performed in a 90 °C oven for 15 minutes and in a 120 °C

oven for 60 minutes. The wafers were then allowed to cool to room temperature at a rate of  $-5\text{ }^{\circ}\text{C}/\text{minute}$  rate.



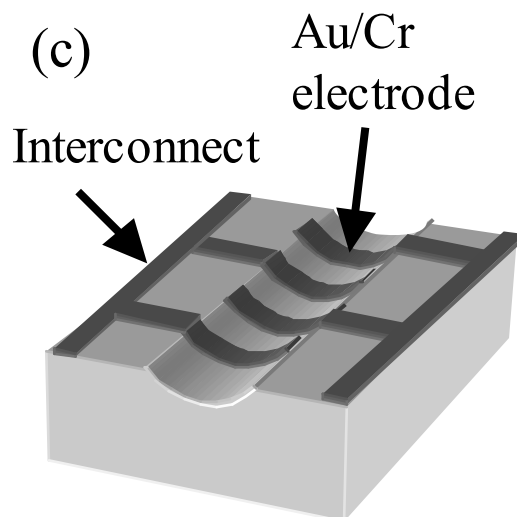


Figure 4.6: A schematic diagram of the fabrication process of the microcylinder

A solution of  $\text{H}_2\text{O}/ 49\% \text{ HF}/ 70\% \text{ HNO}_3/ 37\% \text{ HCl}$  (= 18:2:1:4 by volume) was used to etch the fluidic channel. The etch rate was about  $0.9 \mu\text{m}/\text{min}$  and the etched channels were approximately  $50 \mu\text{m}$  deep and  $250 \mu\text{m}$  wide. The hydrochloric acid in the etchant was used to remove precipitates formed from the reaction of the hydrofluoric acid with alkali metal and alkaline earth constituents in the soda-lime glass in order to obtain a smooth etched surface (Stjernstrom, 1998). The appropriate ratio to ensure a smooth etched surface is about two parts of the 37% HCl in water for one part of the 49 % HF in water.

After the wafers were cleaned with the Piranha and the diluted HF solution,

a 7- $\mu\text{m}$ -thick AZ 9260 photoresist layer was spun onto the wafers. After an 8-minute soft baking procedure at 90 °C, the photoresist was exposed at a dose of 25-mJ/cm<sup>2</sup> to pattern the microelectrode arrays and interconnects. The photoresist was developed in a diluted AZ 400 K developer mixed with AZ 300 MIF developer (1:1 by volume) for 8 minutes, and hard-baked at 90 °C for 10 minutes and subsequently at 120 °C for 40 minutes. The wafers were then dipped into a diluted HF solution (H<sub>2</sub>O: HF = 100:1 by volume) for one minute to create a shallow etched trench that undercuts the photoresist for a subsequent lift-off process. The shallow trench also facilitated the wafer-bonding process because it allowed the wafer surface to remain flat after metal evaporation. This was important because metal lines higher than the surface of the glass wafer can result in defective wafer bonding and leakage from the fluidic channel. For the metal electrodes, a 50-nm-thick chromium and a 150-nm-thick gold film were subsequently deposited using an electron-beam evaporator on the photoresist-patterned wafer. The Cr/Au electrodes were obtained using a lift-off process in acetone. An optical micrograph of the finished channel is shown in Fig. 4.7.

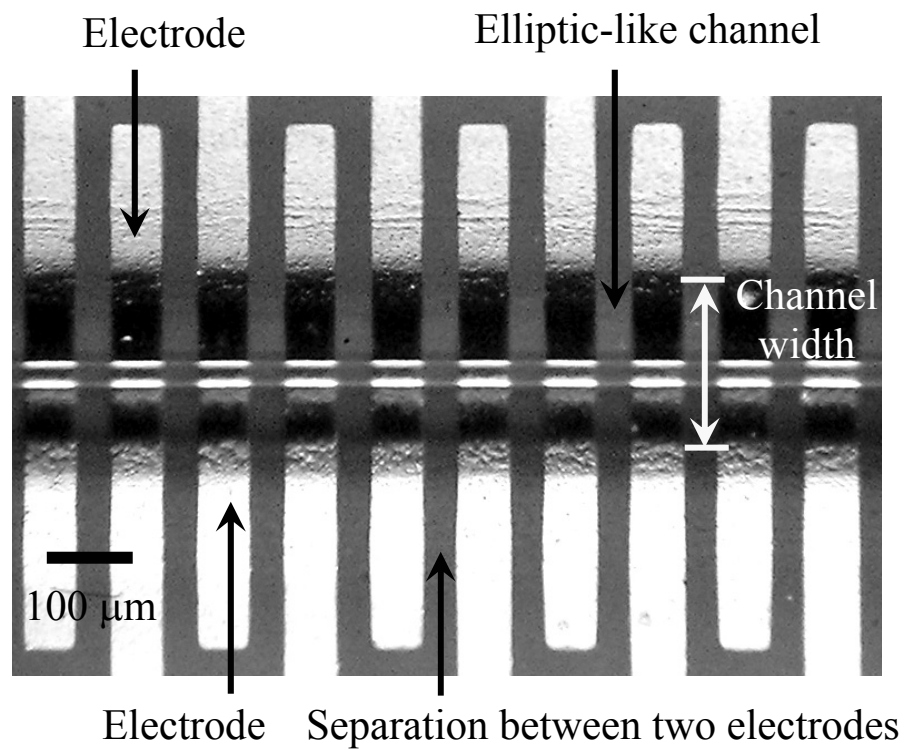


Figure 4.7: An optical micrograph of the elliptic channel with the Au/Cr electrode array

At each end of the channel, a 0.7-mm-diameter hole was drilled for connecting an input or output tube. After the wafers were thoroughly cleaned with the piranha and a diluted HF solution, a small amount of deionized water was applied between the top and bottom wafers. The water layer greatly facilitated wafer alignment by creating a capillary force that prevented the two wafers from

sliding over each other. The aligned wafers were placed between two flat alumina plates to prevent them from adhering to any fixtures during the bonding process, and were pressed by a metal weight in a furnace that was heated with a ramp rate of 10 °C/minute to 670 °C. After 15 minutes, the furnace was cooled down at a rate of approximately -1 °C/minute rate. In the last step, a 0.9 mm outside-diameter plastic tube was inserted into each drilled hole and sealed with epoxy.

#### **4.4. EXPERIMENT**

The focusing capability of the microcytometer using both latex microspheres and cultured HL-60 human leukemia cells has been examined. The width of the particle stream was measured at different amplitudes and frequencies of the applied voltage. The following sections describe the sample preparation, experimental procedures, and results.

##### **4.4.1 Sample preparation**

Fluoresbrite Carboxyl Yellow Green (YG) latex beads (Polysciences, Inc., Warrington, PA product 18142) with a diameter of 10 µm were diluted to a concentration of approximately  $8.5 \times 10^6$  beads/mL in deionized water adjusted to a conductivity of 380 µS/cm with phosphate-buffered saline. HL-60 leukemia cells ( $10^5$  cells/mL) were fluorescently labeled in serum-free RPMI tissue culture medium using a 10 µM concentration of Cell Tracker Green 5-



chloromethylfluorescein diacetate (CMFDA) dye (Molecular Probes, Eugene, OR product C-7025). The cells were incubated with the dye at 37 °C for 30 minutes. During the incubation, the membrane-permeable nonfluorescent CMFDA dye taken up by the cells was modified by cytosolic esterases to yield a fluorescent, membrane-impermeable product (Molecular Probes Inc., OR). Labeled cells were pelleted by centrifugation at 480g relative centrifugal force (RCF) for 10 minutes, resuspended in fresh RPMI medium, and incubated for an additional 20 minutes at 37 °C to ensure complete dye modification. Cells were then pelleted and resuspended at a concentration of  $10^5$  cells/mL in degassed 8.5% (w/v) sucrose, 0.3% (w/v) dextrose solution adjusted to a conductivity of 560  $\mu$ S/cm.

#### **4.4.2 Experimental procedure and results**

A schematic diagram of the experimental setup is shown in Fig. 4.8. A function generator was used to apply an AC sinusoidal voltage to the microelectrodes. A syringe pump was connected to one of the two tubes to inject the suspension of microbeads or leukemia cells into the microfluidic channel, which was located on the stage of an epifluorescent microscope (Zeiss Axiovert S100). The microscope was configured to illuminate the channel with blue light at several points along the flow path. The fluorescently labeled particles were excited by the blue light to emit green fluorescence. The trajectory of the particle stream was recorded using a CCD camera (Hamamatsu C2400-08) connected to

the microscope.

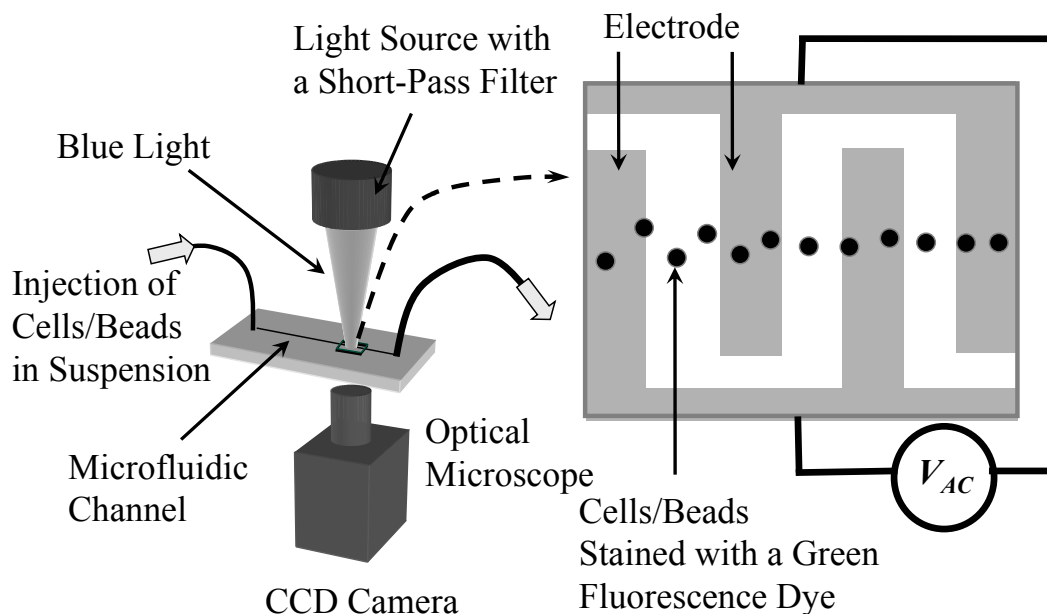
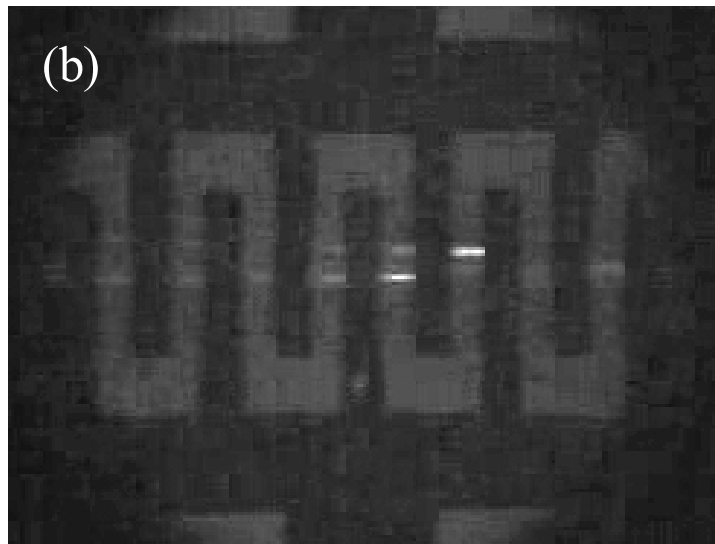
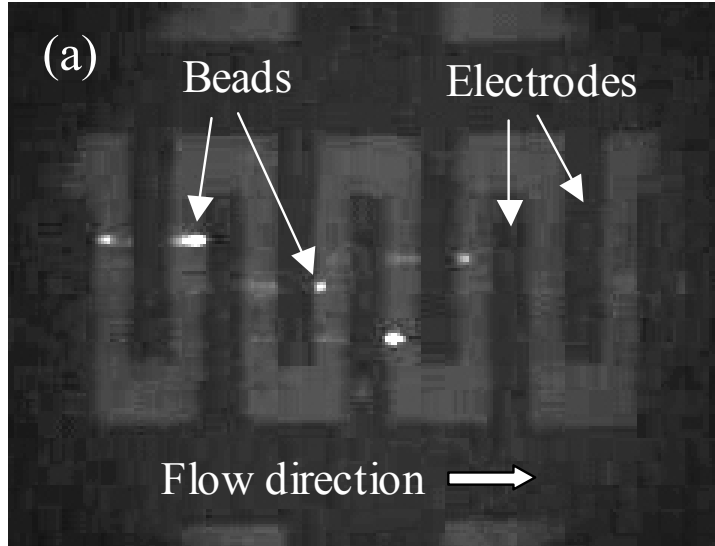


Figure 4.8: A schematic diagram of the experimental setup for measuring the width of the particle stream

A  $15 V_{p-p}$ , 10 kHz voltage was applied to the microelectrodes as the suspension flowed through the channel with approximately 0.45 mm/sec mean flow velocity. It was clearly observed that the particles were focused and scattered in the channel as the applied voltage was repeatedly turned on and off. Figure 4.9 shows a fluorescence micrograph of a portion of the channel. Without an applied voltage, the particles were scattered randomly over the channel (Fig. 4.9a).



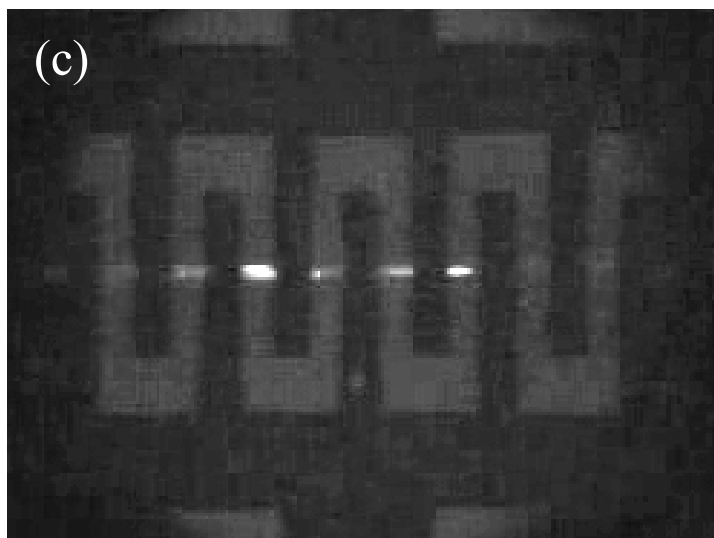


Figure 4.9: Fluorescence micrographs of the microfluidic channel as particles flow along the channel. (a) No electric field is applied; (b) Particle focusing is initiated after an electric field is applied; (c) Particles are tightly focused at the center of the microfluidic channel.

As soon as the electric voltage was applied to the electrodes, the width of the particle stream was narrowed as the particles traveled along the channel (Fig. 4.9b). Figure 4.9c shows that the particles are very tightly focused at the center of the channel. This tight focusing occurred after the suspension flowed through just the first 2 mm section of the 10-mm-long channel.

To verify that the particle was indeed focused by a negative dielectrophoretic force, the frequency of the applied field was varied. When the frequency was 200 Hz and a medium conductivity of approximately  $0.2 \mu\text{S/cm}$ ,

the latex beads could not be focused. This observation agrees with our calculation results shown in case c of Fig. 4.2 that the dielectrophoretic force is positive at this frequency and cannot be used to focus the latex beads. Additionally, the leukemia cells could not be focused at a frequency much higher than 100 kHz, indicating that the Clausius-Mossotti factor becomes positive or close to zero at high frequencies, in agreement with case a of Fig. 4.3. The frequency dependence would suggest that the focusing observed for the beads and cells at the frequency window of 2-100 kHz was not due to other effects such as Joule-heating of the medium. Moreover, the temperature rise due to Joule-heating could be estimated as  $\Delta T \approx \sigma V_{rms}^2 / k$  (Ramos, 1998), where  $\sigma$  and  $k$  are the electrical conductivity and the thermal conductivity of the medium, respectively. For  $\sigma = 380 \mu\text{S/cm}$ ,  $V_{rms} = 5.3 \text{ V}$ ,  $k = 0.6 \text{ J m}^{-1}\text{s}^{-1}\text{K}^{-1}$ , the temperature rise is only on the order of 2 °C. This small temperature rise would not be sufficient to focus particles via a thermal diffusion or thermocapillary effect.

The width of the focusing stream was measured when the amplitude of the applied voltage was varied from 0 to 20 V at three different frequencies, 10, 30, and 100 kHz. The measurement was performed using the captured video images of the fluorescence microscope with the 100  $\mu\text{m}$  center-to-center distance between two adjacent electrodes (shown in Fig. 4.7) as a calibration. The mean flow velocity during the experiments with the latex beads and the leukemia cells

was approximately 2.7 mm/sec and 1.2 mm/sec, respectively. The maximum width of the recorded particle stream for approximately 20 seconds at a specific frequency and voltage was measured and plotted in Fig. 4.10 for the microbeads and in Fig. 4.11 for the cells as a function of applied voltage at the three different frequencies. Although the width of the particle streams at the three different frequencies varies in the low voltage range, it steadily decreases with the applied voltages at any specific frequency. On the other hand, at voltages below 5 V, the dielectrophoretic force is too weak to hold the particles at the center of the channel because the dielectrophoretic force falls exponentially with the distance from the edges of the electrodes (Wang, 1998).

At a voltage of 15  $V_{p-p}$ , there was no signatures indicating cell damage. According to the investigation by Forster *et al.* (1985) and Muller *et al.* (2003) on the effect of an electric field on cell viability, yeast cells were not damaged by exposure in an electric field of up to approximately  $7 \times 10^5$  V/m. At an applied voltage of 15  $V_{p-p}$ , the maximum voltage difference between the two adjacent electrodes in our focusing channel is 7.5 V. As shown in Fig. 5, the field strength is below  $7 \times 10^5$  V/m at most part of the channel when a voltage of 7.5 V is applied. Thus, the field strength is expected to be below the threshold for damaging the cell. Additionally, Wang *et al.* (1999) investigated the effect of electric field on cell viability. They found that an accumulation of electrochemically-generated

peroxide in the suspending medium could account for cell damage, but can be eliminated by the addition of catalase to the suspending medium. In the fluidic device, the medium is continually refreshed and thereby the peroxide accumulation would be negligible. In the focusing channel, furthermore, the cells were moved away from the high field region very quickly into the center with the minimum field strength. Hence, cells could be focused without damaging cells, sufficiently small for cytometry applications at a voltage of about 15  $V_{p-p}$ .

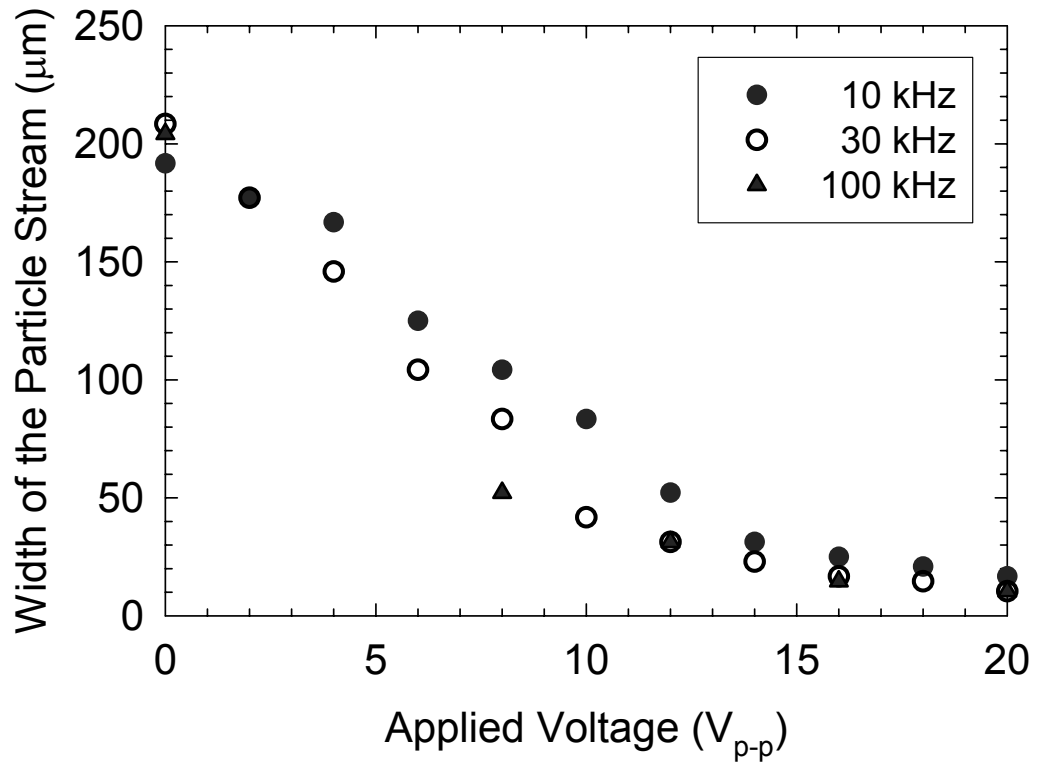


Figure 4.10: The width of a flow stream of microbeads as a function of the applied voltage at different frequencies



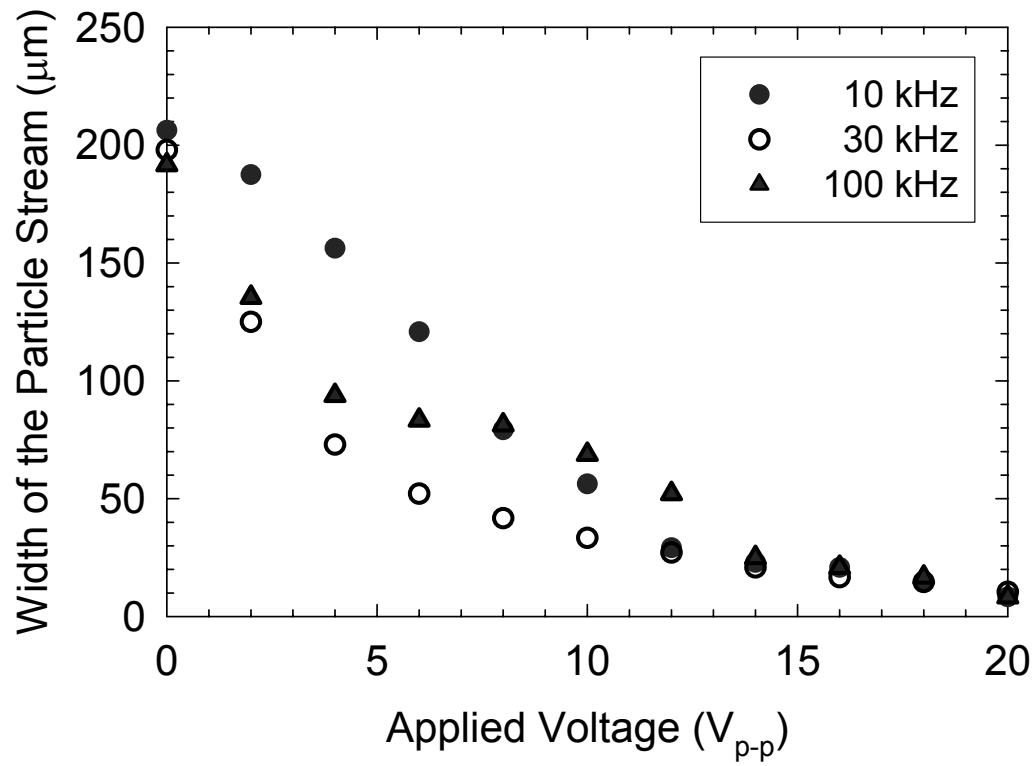


Figure 4.11: The width of a flow stream of human leukemia cells as a function of the applied voltage at different frequencies

## Chapter 5: Conclusion

The thermophysical properties of 1D nanostructures including nanotubes have been measured using a batch-fabricated microdevice. The device has been used to obtain the thermal conductance, electrical conductance, and Seebeck coefficient of the sample. The thermoelectric figure of merit of the sample has been obtained from these measured properties.

The measurements were performed in an evacuated liquid helium cryostat spanning a temperature range of 4-400 K. The sensitivity in thermal conductance measurement is estimated to be on the order of  $10^{-10}$  and  $10^{-9}$  W/K at 30 and 300 K, respectively. Errors due to radiation is estimated to be less than  $8 \times 10^{-14}$  and  $7 \times 10^{-11}$  W/K at 30 K and 300 K, respectively; while conduction through residual gas molecules contributed to less than  $2 \times 10^{-12}$  W/K at 300 K. The TCR of the PRT became smaller at temperatures below 30 K, and it is necessary to use other high-TCR materials such as Nb doped Si to replace the PRT in order to reduce the measurement uncertainty at low temperatures.

The measurement results of an individual 1~3-nm-diameter SWCN, a 10-nm-diameter SWCN bundle, and a 148-nm-diameter SWCN bundle were presented. The measurement results showed that the thermal conductivity of the individual SWCN was higher than those of an individual MWCN and SWCN

bundles due to the absence of inter-tube and inter-shell phonon scattering. The observed thermal conductivities of the bundles were suppressed due to phonon scattering at many defects and contacts. The accurate diameter of the individual SWCN needs to be measured using TEM.

The microdevice has also been integrated with single crystalline metal oxide nanobelt for detecting gas species. The nanobelts were assembled on the microdevice using either electric-field assisted trapping via positive dielectrophoresis or a wet-deposition method. The micro-gas sensor has been tested for NO<sub>2</sub>, ethanol, and DMMP gas species at different concentration. To enhance its sensitivity, the microdevice was heated with a power consumption of only 2.2 mW up to 400 °C. The sensor showed fast response and high sensitivity. Furthermore, as soon as the gas species were removed, the conductance of the belt fully recovered in only few minutes. The high repeatability and stability of the SnO<sub>2</sub> nanobelt is due to its single crystalline structure without grain boundaries. As a result, the nanobelt sensor eliminates the grain boundary poisoning effect that has limited the usage of metal-oxide based sensor.

While this directed assembly approach can enable one to combine nanomaterials synthesis with MEMS fabrication for the large-scale manufacturing of integrated nano-sensor systems, the electric field manipulation has also been used for micro-cytometry applications. The micro-cytometer consists of a unique

electrode design that generates a nonuniform electric field to focus a stream of cells toward the center of a microfluidic channel from all directions by a negative dielectrophoretic force. Large negative dielectrophoretic forces can be obtained for cell focusing by using an AC voltage of a frequency below 100 kHz, where the width of the focused particle stream only weakly depends on the frequency and can be narrowed sufficiently for the cytometer application by increasing the amplitude of the voltage to about  $15 V_{p-p}$  without causing cell death. Latex microbeads and human leukemia cells have been focused within a width of 10-15  $\mu\text{m}$  without the use of a complicated hydrodynamic focusing system.

Moreover, an analysis using a thin shell model indicates that other biological cells can also be focused in the microcytometer as their membrane conductance usually falls within the range of 20~2000  $\text{S}/\text{m}^2$ . This design eliminates the sheath flow and the fluid control system that makes conventional cytometers bulky, complicated, and difficult to operate, and offers the advantages of a portable module that could potentially be integrated with an on-chip impedance or optical sensors into a micro total analysis system.

## BIBLIOGRAPHY

- Altendorf, E., Zebert, D., Holl, M., and Yager, P., 1997, "Differential Blood Cell Counts Obtained Using a Microchannel Based Flow Cytometer," in *Proc. IEEE Int. Conf. on Solid-State Sensors and Actuators*, Chicago, IL, pp. 531-534.
- Anothainart, K., Burgmair, M., Karthigeyan, A., Zimmer, M., Eisele, I., 2003, "Light Enhanced NO<sub>2</sub> Gas Sensing with Tin Oxide at Room Temperature: Conductance and Work Function Measurements," *Sens. Actuators B*, vol. 93, pp. 580-584.
- Arnold, W. M., Schwan, H. P., and Zimmermann, U., 1987, "Surface Conductance and Other Properties of Latex Particles Measured by Electrorotation," *J. Phys. Chem.*, vol. 91, pp. 5093-5098.
- Berber, S., Kwon, Y.-K., and Tomanek, D., 2000, "Unusually High Thermal Conductivity of Carbon Nanotubes," *Phys. Rev. Lett.*, vol. 84, pp. 4613-4616.
- Bockrath, M., Cobden, D.H., Lu, J., Rinzler, A.G., Smalley, R.E., Balents, and L., McEuen, P.L., 1999, "Luttinger-liquid Behavior in Carbon Nanotubes," *Nature*, vol. 397, pp. 598-601.
- Bradley, K., Jhi S.-H., Collins, P.G., Hone, J., Cohen, M.L., Louie S.G., and Zettl, A., 2000, "Is the Intrinsic Thermoelectric Power of Carbon Nanotubes Positive?" *Phys. Rev. Lett.*, vol. 85, pp. 4361-4364.
- Cahill, D. G., 1990, "Thermal Conductivity Measurement from 30-750 K: The  $3\omega$  Method," *Review of Scientific Instruments*, vol.61, pp. 802-808.
- CellTracker™ Probes for Long-Term Tracing of Living Cells*, Molecular Probes Inc., Eugene, OR, 2003.

- Che, J., Cagin, T., and Goddard, W. A., 2000, "Thermal Conductivity of Carbon Nanotubes," *Nanotechnology*, vol. 11, pp. 65-69.
- Chen, X. Q., Saito, T., Yamada, H., and Matsushige, K., 2001, "Aligning Single-Wall Carbon Nanotubes with an Alternating-Current Electric Field," *Appl. Phys. Lett.*, vol. 78, pp. 3714.
- Cheung, K., Gawad, S., and Renaud, P., 2004, "Microfluidic Impedance Spectroscopy Flow Cytometer: Particle Size Calibration," in *Proc. IEEE Int. Conf. on Micro Electro Mechanical Systems*, Maastricht, The Netherlands, pp. 343-346.
- Collins, P.G., Bradley, K., Ishigami, M., and Zettl A., 2000, "Extreme Oxygen Sensitivity of Electrical Properties of Carbon Nanotubes," *Science*, vol. 287, pp. 1801-1804.
- Comini, E.; Faglia, G.; Sberveglieri, G.; Pan, Z. W.; Wang, Z. L., 2002, "Stable and Highly Sensitive Gas Sensors Based on Semiconducting Oxide Nanobelts" *Appl. Phys. Lett*, vol. 81, pp. 1869.
- Cui, Y.; Wei, Q.; Park, H.; Lieber, C. M., 2001, "Nanowire Nanosensors for Highly Sensitive and Selective Detection of Biological and Chemical Species" *Science*, vol. 293, pp. 1289-1292.
- Dai, Z. R.; Pan, Z. W.; Wang, Z. L., 2003, "Novel Nanostructures of Functional Oxides Synthesized by Thermal Evaporation" *Advanced Functional Materials*, vol.13, pp. 9-13.
- De Vecchio, D., Taborek, P., and Rutledge, J.E., 1995, "Matching the Resistivity of Si:Nb Thin Film Thermometers to the Experimental Temperature Range," *Rev. Sci. Instrum.*, Vol. 66, pp. 5367-5368.
- Ding, J., McAvoy, T. J., Cavicchi, R. E., Semancik, S., 2001, "Surface State Trapping Models for SnO<sub>2</sub>-Based Microhotplate Sensors," *Sens. Actuators B*, vol. 77, pp. 597-613.

- Dresselhaus, M. S. and Eklund, P. C., 2000, "Phonons in Carbon Nanotubes," *Advances in Physics*, vol. 49(6), pp. 705-814.
- Duan, X.; Huang, Y.; Cui, Y.; Wang, J.; Lieber, C. M., 2001, "Indium Phosphide Nanowires as Building Blocks for Nanoscale Electronic and Optoelectronic Devices," *Nature*, vol. 409, 66-69.
- Fiedler, S., Shirley, S. G., Schnelle, T., and Fuhr, G., 1998, "Dielectrophoretic Sorting of Particles and Cells in a Microsystem," *Anal. Chem.*, vol. 70, pp. 1909-1915.
- Forster, E., and Emeis, C. C., 1985, "Quantitative Studies on the Viability of Yeast Protoplasts Following Dielectrophoresis," *FEMS Microbiology Letters*, vol. 26, pp. 65-69.
- Fuhr, G., Arnold, W. M., Hagedorn, R., Muller, T., Benecke, W., Wahner, B., and Zimmermann, U., 1992, "Levitation, Holding, and Rotation of Cells within Traps Made by High-Frequency Fields," *Biochim. Biophys. Acta*, vol. 1108, pp. 215-223.
- Gardner, J. W., *(Bio)chemical Microsensors, in Microsensors: Principles and Applications*, John Wiley and Sons, West Sussex, UK, 1994; p 224
- Gascoyne, P. R. C., Becker, F. F., and Wang, X.-B., 1995, "Numerical Analysis of the Influence of Experimental Conditions on the Accuracy of Dielectric Parameters Derived from Electrorotation Measurements," *Bioelectrochem. Bioenerg.*, vol. 36, pp. 115-125.
- Gascoyne, P. R. C., Wang, X.-B., Huang, Y., and Becker, F. F., 1997, "Dielectrophoretic Separation of Cancer Cells from Blood," *IEEE Trans. Ind. Applicat.*, vol. 33, pp. 670-678.
- Holmes, D., Morgan, H., and Thomas, M. R., 2000, "Dielectrophoretic Separation/Isolation of Rare Particles/Cell Types Form a Heterogeneous

Suspension within a Microfluidic System,” in *Proc. the mTAS Symposium*, Enschede, Netherlands, pp. 115-118.

Hone, J., Ellwood, I., Muno, M., Mizel, A., Cohen, M.L., Zettl, A., Rinzler, A.G., and Smalley, R.E., 1998, “Thermoelectric Power of Single-Walled Carbon Nanotubes,” *Physical Review Letters*, vol. 80, pp. 1042-1045.

Hone, J., Whitney, M., Piskoti, and Zettl, A., 1999, “Thermal Conductivity of Single-Walled Carbon Nanotubes,” *Physical Review B*, vol. 59, pp. R2514-2516.

Hone, J., Llaguno, M.C., Nemes, N.M., Johnson, A.T., Fischer, J.E., Walters, D.A., Casavant, M.J., Schmidt, J., Smalley, R.E., 2000, “Electrical and Thermal Transport Properties of Magnetically Aligned Single Wall Carbon Nanotube Films,” *Applied Physics Letters*, vol. 77, pp. 666-668.

Huang, Y., Wang, X.-B., Tame, J. A., and Pethig, R., 1993, “Electrokinetic Behaviour of Colloidal Particles in Travelling Electric Fields: Studies Using Yeast Cells,” *J. of Phys. D: Appl. Phys.*, vol. 26, pp. 1528-1535.

Hughes, M. P., Morgan, H., Rixon, F. J., Burt, J. P. H., and Pethig, R., 1998, “Manipulation of Herpes Simplex Virus Type 1 by Dielectrophoresis,” *Biochim. Biophys. Acta*, vol. 1425, pp. 119-126.

Hughes, W. and Wang, Z. L., 2003, “Nanobelts as Nanocantilevers,” *Appl. Phys. Lett.*, vol. 82, pp. 2886-2888.

Huh, D., Tung, Y.-C., Wei, H.-H., Growtherg, J. B., Skerlos, S. J., Kurabayashi, K., and Takayama, S., 2002, “Use of Air-liquid Two-Phase Flow in Hydrophobic Microfluidic Channels for Disposable Flow Cytometers,” *Biomedical Microdevices*, vol. 4(2), pp. 141-149.

Jones, T. B., *Electromechanics of Particles*, New York: Cambridge University Press, 1995, ch. 2-3.



- Kim, P., Shi, L., Majumdar, A., and McEuen, P. L., 2001, "Thermal Transport Measurements of Individual Multiwalled Nanotubes," *Phy. Rev. Lett.*, vol. 87, pp. 215502/1-215502/4.
- Kovacs, G. T. A., *Micromachined Transducers Sourcebook*, McGraw-Hill, Boston, 1998.
- Lantto, V., Rantala, T. T., Rantala, T. S. 2001, "Atomistic Understanding of Semiconductor Gas Sensors," *J. European Ceramic Society*, vol. 21, pp. 1961–1965.
- Lee, G.-B., Hung, C.-I., Ke, B.-J., Huang, G.-R., Hwei, B.-H., and Lai, H.-F., 2001, "Hydrodynamic Focusing for a Micromachined Flow Cytometer," *ASME J. of Fluids Engineering*, vol. 123, pp. 672 –679.
- Li, D., Wu, Y., Fan, R., Yang, P., and Majumdar, A., 2003a, "Thermal Conductivity of Si/SiGe Superlattice Nanowires," *Applied Physics Letters*, vol. 83(15), pp. 3186-3188.
- Li, D., Wu, Y., Kim, P., Shi, L., Yang, P., and Majumdar, A., 2003b, "Thermal Conductivity of Individual Silicon Nanowires," *Applied Physics Letters*, vol. 83(14), pp. 2934-2936.
- Melamed, M. R., Lindmo, T., and Mendelsohn, M. L., *Flow Cytometry and Sorting*, New York: Wiley, 1991, ch. 1.
- Mizel, A., Benedict, L. X., Cohen, M. L., Louie, S. G., Zettl, A., Budraa, N. K., Beyermann, W. P., 1999, "Analysis of the Low-Temperature Specific Heat of Multiwalled Carbon Nanotubes and Carbon Nanotube Ropes," *Physical Review B*, vol. 60, pp. 3264-3270.
- Morgan, H., Holmes, D., and Green, N.G., 2003, "3D Focusing of Nanoparticles in Microfluidic Channels," in *Proc. IEE Nanobiotechnol.*, vol. 159(2), pp. 76-81.

- Morgan, H., Hughes, M. P., and Green, 1999, N. G., "Separation of submicron bioparticles by dielectrophoresis," *Biophys. J.*, vol. 77, pp. 516–525.
- Morrison, S. R., *Chemical Sensors, in Semiconductor Sensors*, John Wiley and Sons, New York, NY, 1994.
- Muller, T., Pfennig, A., Klein, P., Gradl, G., Jager, M., and Schnelle, T., 2003, "The Potential of Dielectrophoresis for Single-cell Experiments," *IEEE Engineering in Medicine and Biology Magazine*, vol. Nov./Dec., pp. 51-61.
- Noh, H. S.; Hesketh, P. J.; Frye-Mason, G. C., 2002, "Parylene Gas Chromatographic Column for Rapid Thermal Cycling," *J. Microelectromechanical Systems*, vol. 11, pp. 718-725.
- Novak, J. P., Snow, E. S., Houser, E. J., Park, D., Stepnowski, J. L., and McGill, R. A., 2003, "Nerve Agent Detection Using Networks of Single-walled Carbon Nanotubes," *Applied Physics Letters*, vol. 83 (19), pp. 4026-4028.
- Oh, S. W.; Kim, Y. H.; Yoo, D. J.; Oh, S. M.; Park, S. J., 1993, "Sensing Behaviour of Semiconducting Metal Oxides for the Detection of Organophosphorus Compounds," *Sensors and Actuators B*, vol. 13-14, pp.400-403.
- Ormerod, M. G., *Flow Cytometry*, New York: Oxford University Press, 2000, ch. 1.
- Pan, Z. W.; Dai, Z. R.; Wang, Z. L., 2001, "Nanobelts of Semiconducting Oxides," *Science*, vol. 291, 1947-1949.
- Pohl, H. A., *Dielectrophoresis*, London, UK: Cambridge University Press, 1978, ch. 1.

- Pethig, R., Huang, Y., Wang, X., and Burt, J., 1992, "Positive and Negative Dielectrophoretic Collection of Colloidal Particles Using Interdigitated Castellated Microelectrodes," *J. Phys. D: Appl. Phys.*, vol. 24, pp. 881-888.
- Ramos, A., Morgan, H., Green, N. G., and Castellanos, A., 1998, "Ac Electrokinetics: A Review of Forces in Microelectrode Structures," *J. Phys. D: Appl. Phys.*, vol. 31, pp. 2338-2353.
- Rowe, D.M., 1995, *CRC Handbook of Thermoelectrics*, CRC Press, New York.
- Scarola, V.W. and Mahan, G.D., 2002, "Phonon Drag Effect in Single-Walled Carbon Nanotubes," *Phys. Rev. B*, vol. 66, pp. 205405.
- Schrum, D. P., Culbertson, C. T., Jacobson, S. C., and Ramsey, J. M., 1999, "Microchip Flow Cytometry Using Electrokinetic Focusing," *Anal. Chem.*, vol. 71, pp. 4173-4177.
- Schwab, K., Henriksen, E.A., Worlock, J.M.; Roukes, M.L., 2000, "Measurement of the Quantum of Thermal Conductance," *Nature*, vol. 404, pp. 974-976.
- Shi, L., Li, D., Yu, C., Jang, W., Yao, Z., Kim, P., and Majumdar, A., 2003, "Measuring Thermal and Thermoelectric Properties of One-Dimensional Nanostructures Using a Microfabricated Device," *Journal of Heat Transfer*, vol. 125, pp. 881-888.
- Shim, M.; Wong, N.; Kam, S.; Chen, R. J.; Li, Y.; Dai, H., 2002, "Functionalization of Carbon Nanotubes for Biocompatibility and Biomolecular Recognition," *Nano Lett.*, Vol. 2 (4), pp. 285-288.
- Smith, P. A., Nordquist, C. D.; Jackson, T. N.; Mayera, T. S.; Martin, B. R.; Mbindyo, J.; Mallouk, T. E., 2000, "Electric-Field Assisted Assembly and Alignment of Metallic Nanowires," *Appl. Phys. Lett.*, vol. 77, pp. 1399-1401.

- Stjernstrom, M. and Roeraade, J., 1998, "Method for Fabrication of Microfluidic Systems in Glass," *J. Micromech. Microeng.*, vol. 8, pp. 33-38.
- Tian, W.-C.; Pang, S.W.; Lu, C.-J.; Zellers, E. T., 2003, "Microfabricated Preconcentrator-Focuser for a Microscale Gas Chromatograph," *J. Microelectromechanical Systems*, vol. 12, pp. 264-272.
- Wang, T.-H. and Ho, C.-M., 2003, "Nano/Micro Technologies for Single Molecule Manipulation and Detection," in *Proc. IEEE Int. Conf. Robotics and Automation*, Taipei, Taiwan, pp. 3630-3635.
- Wang, X., Becker, F. F., and Gascoyne, P. R. C., 2002, "Membrane Dielectric Changes Indicate Induced Apoptosis in HL-60 Cells More Sensitive than Surface Phosphatidylserine Expression or DNA Fragmentation," *Biochim. Biophys. Acta*, vol. 1564, pp. 412-420.
- Wang, X.-B., Huang, Y., Becker, F. F., and Gascoyne, P. R. C., 1994, "A Unified Theory of Dielectrophoresis and Traveling Wave Dielectrophoresis," *J. Phys. D: Appl. Phys.*, vol. 27, pp. 1571-1574.
- Wang, X.-B., Huang, Y., Vykoukal, J., Becker, F. F., and Gascoyne, P.R.C., 2000, "Cell Separation by Dielectrophoretic Field-Flow-Fractionation," *Anal. Chem.*, vol. 72, pp. 832-839.
- Wang, X.-B., Vykoukal, J., Becker, F. F., and Gascoyne, P. R. C., 1998, "Separation of polystyrene microbeads using dielectrophoretic /gravitational field-flow-fractionation," *Biophys. J.*, vol. 74, pp. 2689-2701.
- Wang, X., Yang, J., and Gascoyne, P. R. C., 1999, "Role of peroxide in AC electrical field exposure effects on Friend murine erythroleukemia cells during dielectrophoretic manipulations," *Biochim. Biophys. Acta*, vol. 1426, pp. 53-68.
- Yang, J., Huang, Y., Wang, X., Wang, X.-B., Becker, F. F., and Gascoyne, P. R. C., 1999, "Dielectric Properties of Human Leukocyte Subpopulations

Determined by Electrorotation as a Cell Separation Criterion,” *Biophys. J.*, vol. 76, pp. 3307-3314.

Yao, Z., Postma, H.W.Ch., Balents, L., and Dekker, C., 1999, “Carbon Nanotube Intramolecular Junctions,” *Nature*, vol. 402, pp. 273-280.

Yi, W., Lu, L., Zhang D. L., Pan, Z. W., and Xie, S. S., 1999, “Linear Specific Heat of Carbon Nanotubes,” *Physical Review B*, vol. 59, pp. R9015-9018.

## **Vita**

Choongho Yu was born in Seoul, Korea, in 1971, the son of Sungsoo Yu and Soonjoo Lee. After completing his work at Daeil Foreign Language High School, Seoul, Korea, in February 1990, he entered Korea University in Seoul, Korea. After serving military service from 1992 to 1993, he received the degree of Bachelor of Science from Korea University in February 1997. He entered the Graduate School of Korea University, Seoul, Korea, in March 1997 and received the degree of Master of Science from Korea University in February 1999. In August 1999, he entered the doctoral program in Mechanical Engineering Department at The University of Texas at Austin.

Permanent address: 514-13 Shillim 4-dong Kwanak-gu Seoul, Korea

This dissertation was typed by the author.